



**HAL**  
open science

## Thermal history of Northwest Africa 5073–A coarse-grained Stannern-trend eucrite containing cm-sized pyroxenes and large zircon grains

Julia Roszjar, Knut Metzler, Addi Bischoff, Jean-Alix J-A Barrat, Thorsten Geisler, R.C. Greenwood, I. A. Franchi, Stephan Klemme

► **To cite this version:**

Julia Roszjar, Knut Metzler, Addi Bischoff, Jean-Alix J-A Barrat, Thorsten Geisler, et al.. Thermal history of Northwest Africa 5073–A coarse-grained Stannern-trend eucrite containing cm-sized pyroxenes and large zircon grains. *Meteoritics and Planetary Science*, 2011, 46 (11), pp.1754-1773. 10.1111/j.1945-5100.2011.01265.x . insu-00637903

**HAL Id: insu-00637903**

**<https://insu.hal.science/insu-00637903>**

Submitted on 3 Apr 2012

**HAL** is a multi-disciplinary open access archive for the deposit and dissemination of scientific research documents, whether they are published or not. The documents may come from teaching and research institutions in France or abroad, or from public or private research centers.

L'archive ouverte pluridisciplinaire **HAL**, est destinée au dépôt et à la diffusion de documents scientifiques de niveau recherche, publiés ou non, émanant des établissements d'enseignement et de recherche français ou étrangers, des laboratoires publics ou privés.

1                   **Thermal history of Northwest Africa (NWA) 5073**  
2    **- a coarse-grained Stannern-trend eucrite containing cm-sized pyroxenes**  
3                   **and large zircon grains**  
4  
5  
6  
7

8           **Julia Roszjar<sup>1</sup>, Knut Metzler<sup>1</sup>, Addi Bischoff<sup>1</sup>, Jean-Alix Barrat<sup>2</sup>, Thorsten Geisler<sup>3</sup>,**  
9           **Richard C. Greenwood<sup>4</sup>, Ian A. Franchi<sup>4</sup>, and Stephan Klemme<sup>5</sup>**

10  
11    <sup>1</sup>Institut für Planetologie, Westfälische Wilhelms-Universität Münster, Wilhelm-Klemm-Str. 10, D-  
12    48149 Münster, Germany (e-mail: j\_rosz01@uni-muenster.de).  
13

14    <sup>2</sup>Université Européenne de Bretagne, Institut Universitaire Européen de la Mer, Place Nicolas  
15    Copernic, 29280 Plouzané Dedex, France.  
16

17    <sup>3</sup>Steinmann Institut, Rheinische Friedrich-Wilhelms-Universität Bonn, Poppelsdorfer Schloß, 53115  
18    Bonn, Germany  
19

20    <sup>4</sup>Planetary and Space Sciences Research Institute, The Open University, Milton Keynes, MK7 6AA,  
21    UK.  
22

23    <sup>5</sup>Institut für Mineralogie, Westfälische Wilhelms-Universität Münster, Corrensstr. 24, D-48149  
24    Münster, Germany.  
25  
26  
27  
28  
29  
30  
31  
32  
33  
34  
35  
36  
37  
38  
39  
40  
41  
42  
43  
44  
45  
46  
47  
48  
49  
50  
51

52 **Abstract**

53 We report on the bulk chemical composition, petrology, oxygen isotopic composition, trace  
54 element composition of silicates, and degree of self-irradiation damage on zircon grains of the eucrite  
55 Northwest Africa (NWA) 5073, to constrain its formation and post-crystallization thermal history, and  
56 to discuss their implications for the geologic history of its parent body. This unequilibrated and  
57 unbrecciated meteorite is a new member of the rare Stannern-trend eucrites. It is mainly composed of  
58 elongated, zoned pyroxene phenocrysts up to 1.2 cm, plagioclase laths up to 0.3 cm in length, and is  
59 rich in mesostasis. The latter contains zircon grains up to 30  $\mu\text{m}$  in diameter, metal, sulfide, tridymite,  
60 and Ca-phosphates. Textural observations and silicate compositions coupled with the occurrence of  
61 extraordinary Fe-rich olivine veins that are restricted to large pyroxene laths indicate that NWA 5073  
62 underwent a complex thermal history. This is also supported by the annealed state of zircon grains  
63 inferred from  $\mu$ -Raman spectroscopic measurements along with U and Th data obtained by electron  
64 probe microanalyses.

65  
66  
67  
68  
69  
70  
71  
72  
73  
74  
75  
76  
77  
78  
79  
80  
81  
82  
83  
84  
85  
86  
87  
88  
89  
90  
91  
92  
93  
94  
95  
96  
97  
98

**Keywords:** eucrite, bulk chemistry, petrology, trace elements, oxygen isotopes,  $\mu$ -Raman spectroscopy, zircon annealing

99 **Introduction**

100           The so-called HED suite of achondrites (Howardites, Eucrites, and Diogenites) makes up the  
101 largest suite of igneous rocks available from any Solar System body besides the Earth and the Moon  
102 (Mittlefehldt et al., 1998). Eucrites represent basaltic rocks and gabbroic cumulates, whereas  
103 diogenites are ultramafic rocks (orthopyroxenites, olivine-bearing orthopyroxenites, harzburgites, and  
104 dunites), mainly composed of orthopyroxene and olivine (e.g., Mittlefehldt et al., 1998; Beck and  
105 McSween, 2010). Howardites are polymict breccias, consisting of various amounts of eucritic and  
106 diogenitic lithologies. The close relationship between HEDs is convincingly supported by  
107 petrographic, mineralogical, chemical, and isotopic evidences (see McSween et al., 2010 for a review),  
108 and suggest that they derived from the same parent body, possibly the asteroid 4 Vesta (e.g., McCord  
109 et al., 1970; Consolmagno and Drake, 1977; Binzel and Xu, 1993; Drake, 2001). However, a few  
110 eucrites display unusual petrographic features and distinct oxygen isotopic compositions and could,  
111 therefore, have originated from distinct parent bodies (e.g., Yamaguchi et al., 2002; Scott et al., 2009;  
112 Gounelle et al., 2009; Bland et al., 2009). Eucrites are widely thought to represent either surface or  
113 near-surface basaltic liquids (lava flows or shallow intrusions) or crystal accumulations from basaltic  
114 liquids. Most eucrites experienced a complex post-crystallization history, including prolonged thermal  
115 metamorphism that produced recrystallization textures and caused exsolution and inversion of  
116 pyroxenes (e.g., Takeda and Graham, 1991; Metzler et al., 1995, Yamaguchi et al., 1996, 2009; Mayne  
117 et al., 2009), and multiple impact events. Thus, many eucrites are brecciated, and were formed in the  
118 regolith and mega-regolith of their parent body (e.g., Stöffler et al., 1988). They consist of mineral  
119 and/or lithic fragments embedded in a fine-grained, generally fragmented matrix (e.g., Takeda and  
120 Graham, 1991; Metzler et al., 1995; Bischoff et al., 2006; Llorca et al., 2009). From a chemical point  
121 of view, eucrites can be subdivided into basaltic (noncumulate), and cumulate eucrites, both of which  
122 occur also as clasts in polymict eucrites and howardites (e.g., Takeda, 1991). Cumulate eucrites are  
123 coarse-grained rocks with high Mg-numbers [ $Mg\# = \text{molar Mg}/(\text{Mg} + \text{Fe})$ ], low incompatible trace  
124 element abundances compared to other eucrites, and pronounced positive Eu anomalies - a feature  
125 consistent with plagioclase accumulation. Basaltic eucrites can be subdivided into three compositional  
126 distinct groups on the basis of their  $Mg\#$  or  $FeO_{\text{total}}/MgO$  wt.% ratio,  $TiO_2$  contents, and incompatible  
127 trace element abundances (e.g., Stolper, 1977; Warren and Jerde, 1987; Mittlefehldt et al., 1998;  
128 Yamaguchi et al., 2009): Main Group Nuevo Laredo-trend eucrites, Stannern-trend eucrites and the  
129 residual eucrites. Main Group Nuevo Laredo-trend eucrites are the most common ones. They display  
130 wide variations in  $Mg\#$  with only moderate variations in incompatible element abundances. They are  
131 believed to represent a fractional crystallization trend (e.g., Stolper, 1977; Warren and Jerde, 1987).  
132 Stannern-trend eucrites are rare. They include three falls (Stannern, Bouvante, and Pomozdino), and  
133 about a dozen finds from Antarctica (e.g., Y-75011) and from the Sahara (e.g., NWA 4523 and NWA  
134 1000). They display the same major element abundances as the less evolved rocks of the Nuevo  
135 Laredo group, but exhibit high Ti and incompatible trace element abundances, and significant negative

136 Eu, Sr, and Be anomalies. The origin of these eucrites is controversial. It has been proposed that the  
137 Stannern-trend eucrites could have been generated from the same mantle source as Main Group  
138 eucrites but at smaller degrees of partial melting, and possibly at slightly different oxygen fugacities  
139 (Stolper, 1977; Mittlefehldt and Lindstrom, 2003). Alternatively, it has been proposed that the high  
140 incompatible trace element abundances could be explained by an intricate in-situ crystallization  
141 process (Barrat et al., 2000), or by the involvement of highly evolved KREEP-like melts (Warren and  
142 Kallemeyn, 2001). The contamination of Main Group eucritic magmas might be also explained by  
143 melts derived from partial melting of the asteroid's crust, which would can successfully explain both  
144 the high incompatible trace elements concentrations and the distinctive Eu, Sr, and Be anomalies  
145 shown by the Stannern-trend eucrites (Barrat et al., 2007). Finally, the residual eucrites display major  
146 element abundances consistent with Main Group eucrites, but light REE depletions and positive Eu  
147 anomalies. Partial melting followed by extraction of a few percent of partial melts can satisfactorily  
148 explain these features (Yamaguchi et al., 2009). At present, it is generally thought that the  
149 differentiation history of the eucrite parent body has been triggered by the formation of a global  
150 magma ocean (e.g., Takeda, 1979; Righter and Drake, 1997; Ruzicka et al., 1997; Warren, 1997;  
151 Greenwood et al., 2005). This hypothesis is at first glance consistent with the petrology of the eucrites,  
152 but cannot easily account for the geochemistry of the diogenites (e.g., Mittlefehldt 2000; Barrat et al.,  
153 2008, 2010). Thus, the magmatic and thermal histories of the parent body were certainly much more  
154 complicated than generally believed and more detailed studies of HED meteorites are necessary to  
155 further our understanding of the process leading to the formation of HED meteorite genesis. Recently,  
156 we have identified NWA 5073, a eucrite which displays some unique features. This single,  
157 unbrecciated stone is characterized by an unusual texture with cm-sized unequibrated pyroxenes  
158 crosscut by numerous secondary olivine-rich veins, and mesostasis areas containing large zircon  
159 grains. Here, we report on the bulk chemistry, petrology, and isotopic characteristics of this  
160 exceptional meteorite and discuss its genesis and complex post-crystallization history. Preliminary  
161 data on NWA 5073 have been previously presented by Roszjar et al. (2009a-c) and Roszjar and  
162 Scherer (2010).

163

## 164 **Analytical Methods**

165 The textural and mineralogical investigations of the sample were performed by optical and  
166 electron microscopy on a thin section (PL07217). Modal abundance of major phases and mesostasis  
167 were determined based on multiple point-counting applied on a backscattered electron (BSE)  
168 photomicrograph using an Olympus Analysis software. A JEOL A840 scanning electron microscope  
169 (SEM) equipped with energy dispersive spectrometers (EDS; INCA; Oxford Instrument) at the  
170 Interdisciplinary Center for Electron Microscopy and Microanalysis (ICEM) at the Westfälische  
171 Wilhelms-Universität Münster was used for detailed petrographic investigations. Qualitative analyses  
172 have been carried out using an acceleration voltage of 20 kV, and a beam current of 15 nA. High

173 contrast, low brightness BSE imaging has been used for systematic identification and localization of  
174 Zr-bearing phases. Quantitative analyses of mineral compositions were obtained using a JEOL JXA  
175 8900 Superprobe electron probe micro analyzer (EPMA) operated at an acceleration voltage and beam  
176 current of 15 kV and 15 nA, respectively. Natural and synthetic standards of well-known compositions  
177 were used as standards. Matrix corrections were made according to the  $\Phi\rho(z)$  procedure of Armstrong  
178 (1991).

179 Prior to micro-Raman spectroscopy, investigations of zircon grains were performed on the  
180 JEOL A840 SEM at conditions described above. BSE imaging allowed selection of 10 appropriate  
181 grains with sufficient diameter ranging from 10-25  $\mu\text{m}$  that were free of cracks and inclusions, and  
182 were representative of the whole zircon population in NWA 5073 in terms of mineral shape and  
183 mineral paragenesis with surrounding phases. The same spots on individual zircon grains investigated  
184 by Raman spectroscopy were subsequently analyzed for major, minor, and trace element  
185 concentrations by wavelength-dispersive analysis using a Cameca SX 100 EPMA at the Institut für  
186 Mineralogie, Universität Hamburg. Major (Si, Zr, Hf) and minor (Al, Fe, P, Ca, Mn, Y) elements were  
187 analyzed in a first sequence using a beam current of 20 nA, an acceleration voltage of 15 keV, total  
188 counting times of 30 s, and a beam diameter of 1-2  $\mu\text{m}$ . Th and U concentrations were subsequently  
189 determined in a separate cycle with total counting times of 600 s ( $10 \times 60$  s) for the U- $M_{\beta}$  and Th- $M_{\alpha}$   
190 line, and a beam current and acceleration voltage of 200 nA and 15 kV, respectively, to achieve a  
191 better precision. A small overlap of the Th- $M_{\alpha}$  on the U- $M_{\beta}$  line was corrected using the method  
192 proposed by Åmli & Griffin (1975). For these conditions the detection limit of U and Th is about 20-  
193 30 ppm.

194 Micro-Raman spectroscopic measurements were performed subsequently, but prior to  
195 compositional analysis by EPMA to preclude any possible irreversible modifications of the radiation-  
196 damaged structure as a result of the electron beam impact. Micro-Raman spectroscopic analyses were  
197 carried out on a polished, cleaned thin section of NWA 5073 using a Jobin Yvon HR800 dispersive  
198 Raman spectrometer at the Institut für Anorganische und Analytische Chemie at the Westfälische  
199 Wilhelms-Universität Münster. The 632.817 nm line of a Nd-YAG laser was used as excitation source  
200 with a beam power of  $\sim 10$  mW at the exit of the laser. The scattered Raman light was collected with a  
201 100 times objective (N.A. = 0.9) with charge-coupled device detector (CCD) after being dispersed by a  
202 grating of 1800 grooves  $\text{mm}^{-1}$ . The spectrometer slit width was set to 150  $\mu\text{m}$ , yielding a spectral  
203 resolution of 1.9  $\text{cm}^{-1}$  near 1000  $\text{cm}^{-1}$  as determined from Ne light bands. The lateral resolution was  
204 about 1-2  $\mu\text{m}$ . A possible spectrometer drift was monitored by measuring the 520.7  $\text{cm}^{-1}$  band of  
205 silicon and the spectral lines of the Ne-lamp immediately before and after the sample analyses.  
206 Information about the structural state of individual zircon grains was obtained by examining the total  
207 spectrum and by monitoring the intensity, full width at half maximum (FWHM), and the frequency of  
208 the internal antisymmetric  $\nu_3(\text{SiO}_4)$  stretching mode located near 1008  $\text{cm}^{-1}$  in a non-metamict zircon.  
209 This band was monitored because (i) it has been shown that it is most suitable for quantifying

210 radiation damage (Wopenka et al., 1996; Nasdala et al., 1996; Nasdala et al., 1998; Palenik et al.,  
211 2003), since it is the strongest Raman band of zircon and thus easy to measure precisely (Dawson et  
212 al., 1971; Nasdala et al., 1996; Zhang et al., 2000a), and (ii) it is not significantly red-shifted by  
213 impurity-related structural disorder such as caused by variations in the Hf concentration (Hoskin and  
214 Rodgers, 1996). The broad band profile in the frequency region between 900 and 1100  $\text{cm}^{-1}$  results  
215 from an overlap of the  $\nu_3(\text{SiO}_4)$  with the adjacent, internal  $\nu_1(\text{SiO}_4)$  stretching mode ( $A_{1g}$  symmetry;  
216 Dawson et al., 1971) at about 975  $\text{cm}^{-1}$  and, in radiation-damaged zircon, from the contribution of a  
217 broad background feature at a lower frequency, which has been assigned to the amorphous component  
218 in metamict zircon (Zhang et al., 2000a). Quantitative band parameters were obtained by  
219 deconvoluting the overall band profile in the frequency region between 800 and 1100  $\text{cm}^{-1}$  with three  
220 Voigt functions and a linear background as shown by Geisler et al. (2001). The reproducibility of the  
221 fitted frequency is better than 0.2  $\text{cm}^{-1}$  and that of the linewidth is in the order of  $\pm 0.5 \text{ cm}^{-1}$  at a  
222 linewidth smaller than 20  $\text{cm}^{-1}$  and  $\pm 1.0 \text{ cm}^{-1}$  for larger linewidths. The effect of the finite slit width on  
223 the measured linewidth, given as the full width at half maximum (FWHM), was then corrected by the  
224 method of Tanabe and Hiraishi (1980).

225 From radioactive decay of the  $^{238}\text{U}$ ,  $^{235}\text{U}$ , and  $^{232}\text{Th}$  isotopes, the number of  $\alpha$ -decay events for  
226 different U and Th concentrations were calculated according to the following equation:

$$227 \quad D_\alpha = 8 N_1 [\exp(\lambda_1 t - 1)] + 7 N_2 [\exp(\lambda_2 t - 1)] + 6 N_3 [\exp(\lambda_3 t - 1)] \quad (1)$$

228 where  $N_1$ ,  $N_2$ , and  $N_3$  are the present concentrations of  $^{238}\text{U}$ ,  $^{235}\text{U}$ , and  $^{232}\text{Th}$  in the zircon grains,  
229 respectively,  $\lambda_1$ ,  $\lambda_2$ , and  $\lambda_3$  are the decay constants for  $^{238}\text{U}$ ,  $^{235}\text{U}$ , and  $^{232}\text{Th}$  in years<sup>-1</sup>, respectively, and  
230  $t$  is the age of the zircon. For our calculations we assumed an age of 4.55 Ga.

231 The bulk chemical composition of NWA 5073 has been determined at the Institut  
232 Universitaire Européen de la Mer (IUEM), Plouzané, using ~100 mg of powdered sample material.  
233 The powdered whole rock fraction, derived from initially ~12 g sample material and devoid of fusion  
234 crust, was precleaned with ethanol and ultra pure MilliQ® water in an ultrasonic bath, before it was  
235 carefully crushed into small pieces in an agate mortar. Subsequently, a representative fraction of 0.48  
236 g was powdered. About 100 mg of the latter were used for bulk rock analyses. Major elements (Ti, Al,  
237 Cr, Fe, Mn, Mg, Ca, Na, K, and P) were determined by ICP-AES (inductively coupled plasma-atomic  
238 emission spectrometry) using the procedure described by Cotten et al. (1995). The accuracy of this  
239 system is better than 5%, and the reproducibility better than 3%. Trace element concentrations were  
240 measured by ICP-MS (inductively coupled plasma-mass spectrometry) using a Thermo Element 2  
241 spectrometer following the procedure described by Barrat et al. (2007). Based on standard  
242 measurements and sample duplicates, trace element concentration reproducibility is generally better  
243 than 5%, except for W, which is generally better than 10%.

244 Trace element abundances of pyroxenes and plagioclases in NWA 5073 were determined by  
245 laser ablation-inductively coupled plasma-mass spectrometry (LA-ICP-MS) at the Institut  
246 Universitaire Européen de la Mer, Plouzané. The analyses were performed under a He atmosphere

247 using an ArF-Excimer (193 nm wavelength) laser ablation system (Geolas Pro102), connected to a  
248 Finnigan Thermo Element 2 spectrometer. Concentrations were determined on individual spots using a  
249 60  $\mu\text{m}$ -diameter laser beam and a laser repetition rate of 10 Hz. Background and peak were measured  
250 for 40 s and 210 s, respectively. For all data, NIST 612 and BCR-2G glass standards were both used  
251 for external calibration of relative element sensitivities, using values given by Jochum et al. (2005).  
252 Replicate analyses of the USGS basaltic-glass standard BIR-1G run at intervals during the analytical  
253 session, yielded an external reproducibility generally better than 5% ( $1\sigma$  relative standard deviation).  
254 Analytical and data reduction procedures followed those described by Barrat et al. (2009). Results  
255 were normalized to CaO abundances measured by electron microprobe as an internal standard to  
256 account for variable ablation yield.

257 Oxygen isotope analysis was carried out at the Open University using an infrared laser  
258 fluorination system (Miller et al., 1999). A 2 mg aliquot of NWA 5073, taken from a larger batch of  
259 homogenized powdered sample material ( $\sim 100$  mg), was loaded in the sample chamber, together with  
260 various international and internal oxygen isotope standards. To maximize yields and decrease the risk  
261 of cross contamination, the powdered sample and standards were fused in vacuum to form a glass bead  
262 prior to fluorination.  $\text{O}_2$  was liberated by heating the glass beads using an infrared  $\text{CO}_2$  laser ( $10.6 \mu\text{m}$ )  
263 in the presence of 210 torr of  $\text{BrF}_3$ . After fluorination, the  $\text{O}_2$  released was purified by passing it  
264 through two cryogenic nitrogen traps and over a bed of heated KBr.  $\text{O}_2$  was analyzed using a  
265 Micromass Prism III dual inlet mass spectrometer. Published system precision ( $1\sigma$ ) (Miller et al.,  
266 1999), based on replicate analyses of international (NBS-28 quartz, UWG-2 garnet) and internal  
267 standards, is approximately  $\pm 0.04\text{‰}$  for  $\delta^{17}\text{O}$ ,  $\pm 0.08\text{‰}$  for  $\delta^{18}\text{O}$ , and  $\pm 0.02\text{‰}$  for  $\Delta^{17}\text{O}$ . Oxygen  
268 isotope analyses are reported in standard  $\delta$ -notation where  $\delta^{18}\text{O}$  has been calculated as:

$$269 \quad \delta^{18}\text{O} = ((\delta^{18}\text{O}/\delta^{16}\text{O})_{\text{sample}}/(\delta^{18}\text{O}/\delta^{16}\text{O})_{\text{ref}}) - 1) \times 1000 \quad (2)$$

270 and similarly for  $\delta^{17}\text{O}$  using  $^{17}\text{O}/^{16}\text{O}$  ratio.  $\Delta^{17}\text{O}$  has been calculated using the linearized format of  
271 Miller (2002):

$$272 \quad \Delta^{17}\text{O} = 1000 \ln (1 + (\delta^{17}\text{O}/1000)) - \lambda 1000 \ln (1 + (\delta^{18}\text{O}/1000)) \quad (3)$$

273 with  $\lambda = 0.5247$ .

274

## 275 **Results**

### 276 *Mineralogy*

277 Northwest Africa 5073 is a desert find with a total mass of 185 g, representing an  
278 unequilibrated, mesostasis-rich basaltic eucrite with the coarsest subophitic to slightly variolitic (fan-  
279 spherulitic) texture among the known eucrites. It is an unbrecciated rock that preserved its  
280 crystallization texture. It is mainly composed of elongated, unequilibrated pyroxene crystals up to 1.2  
281 cm and plagioclase laths up to 0.3 cm in length (Fig. 1). Large phenocrysts of pyroxene make up  
282 approximately 25 vol.% of the whole rock (Table 1). In variolitic areas, the plagioclase tends to be  
283 skeletal, i.e., it occurs as partly hollow crystals, which is indicative of rapid cooling. Euhedral



284 chromite grains, occasionally dendritic, frequently occur with grain sizes up to 0.8 mm. Their  
285 chemical composition (Table 2) is in the range of those for the unequilibrated eucrite Pasamonte  
286 (Mittlefehldt et al., 1998). Fine-grained areas (mesostasis) that make up about 8.5 vol.% of the rock,  
287 occur interstitially to the large crystals (Figs. 1 and 3). Terrestrial weathering of the sample is  
288 indicated by the breakdown of about half of the metals and the occurrence of calcite, and Ba-sulfates  
289 in some cracks all over the thin section. According to the scheme proposed for chondrites by Wlotzka  
290 (1993), NWA 5073 is moderately weathered (W2-3).

291 Large pyroxene crystals are chemically unequilibrated with cores of  $\text{En}_{51-60}\text{Fs}_{34-5}\text{Wo}_{2-8}$  and rims of  
292  $\text{En}_{20-34}\text{Fs}_{42-63}\text{Wo}_{8-34}$  (Figs. 2 and 3; Table 2). The pyroxene composition depicted in Fig. 2, reflects  
293 magmatic zoning from Mg-rich cores to Fe-rich rims of large pigeonite laths adjacent to surrounding  
294 plagioclase crystals, which is typical of more rapidly cooled basalts containing pyroxene that has not  
295 exsolved on a  $\mu\text{m}$  scale, e.g., Y-75011 (Takeda et al., 1994). As emphasized by e.g., Takeda et al.  
296 (1982), chemical zoning in pyroxene primarily depends on the bulk chemistry of the basaltic melt and  
297 on crystal-growth conditions such as the degree of supercooling and nucleation. Re-equilibration of  
298 chemical zoning in pyroxene crystals did not occur in our sample. Thus, NWA 5073 was not formed  
299 in a slow cooling environment, as indicated by the skeletal nature of plagioclases, (see Fig. 3a), and  
300 was not affected by a long-term, high-temperature event, which would have resulted in re-  
301 equilibration of pyroxene crystals. The large pyroxene crystals are frequently twinned and fractured  
302 mainly perpendicular to the c-axis. This is in strong contrast to the adjacent plagioclase crystals which  
303 do not show this fracturing. The small pyroxenes interstitial to the large crystals show similar Ca  
304 contents as the rims of large crystals, but contain somewhat more Fe (Fig. 2, open squares, Table 2).

305 Occasionally, very thin ( $<1\mu\text{m}$ ) exsolution lamellae of augite in the host pyroxenes can be observed  
306 (e.g., Fig. 3). Pyroxenes in contact with the mesostasis frequently have a corroded appearance. Large  
307 pyroxene grains are crosscut by fractures that are mainly filled by Fe-rich olivine. Originating from  
308 these veins, a distinct Fe-enrichment of the adjacent host pigeonite can be observed, which clearly  
309 parallels the veins (Fig. 3). Pyroxene areas distant to these veins appear as Mg-rich “cores”,  
310 surrounded by Fe-enriched areas. These “cores” seem to have preserved their original composition  
311 from primary crystallization ( $\text{Fs}_{\sim 34}$ ). Additionally, Fe has effectively diffused from the olivine veins  
312 and larger fractures devoid of olivine veins into the host pyroxene crystals along certain  
313 crystallographic orientations, which probably represent cleavage plans (see Figs. 3d and 4a-b). Veins  
314 of Fe-rich olivine ( $\text{Fa}_{65-71}$ ) are clearly restricted to the large pyroxene crystals and always end abruptly  
315 at their boundaries. These veins are very irregular with distinct thickness variations (Fig. 3a-c). The  
316 olivine appears to have grown along preexisting fractures of its host pyroxene, while adjacent large  
317 plagioclase crystals are devoid of it (Fig. 3a-c). Euhedral chromite, and troilite crystals, and sporadic  
318 subrounded apatite grains occur within these veins (Fig. 3d). Similar olivine veins have been described  
319 from a few other eucrites and howardites, namely Macibini, Y-7308, Y-790260, Y-75011, Y-82202,

320 NWA 049, NWA 1000, and NWA 2061 (Takeda and Yanai, 1982; Takeda et al., 1983; Metzler, 1985;  
321 Warren, 2002; Barrat et al., 2011).

322 Two primary feldspar generations occur, namely large plagioclase laths (up to 3 mm in length) and  
323 small plagioclase grains located in the mesostasis, both of which are compositionally in the typical  
324 eucrite range (e.g., Mittlefehldt et al., 1998) of  $An_{76-92}Ab_{8-22}Or_{0-3}$  (Fig. 5; Table 2). The plagioclases  
325 found in mesostasis areas tend to be more Ab-rich compared to large plagioclase laths (Fig. 5). Many  
326 large plagioclase crystals are clouded by myriads of exsolved tiny pyroxene and  $SiO_2$  grains, as  
327 commonly observed in eucrites (e.g., Harlow and Klimentidis, 1980; Metzler et al., 1995). Additional  
328 to the primary plagioclases, we identified another, probably second generation of feldspars that are  
329 typically  $An_{97-100}$  in composition (Fig. 5) and were usually found in association with Fe-rich olivine  
330 veins within large pyroxene laths (Fig. 4).

331 The mesostasis consists of tridymite laths up to 0.8 mm, Ni-poor metallic Fe ( $<300 \mu m$ ), ilmenite ( $<60$   
332  $\mu m$ ), chromite, plagioclase, augite, apatite, merrillite, troilite, zircon, baddeleyite, and very small  
333 amounts of Fe-rich olivine. In addition, sporadic anorthite ( $An_{95}$ ) was found. In some cases the  
334 mesostasis areas are not well-defined and appear blurred. More than 30 grains of Zr-bearing phases,  
335 such as zircon, baddeleyite, and zirconolite grains, with diameters ranging from 1 to 30  $\mu m$  were  
336 found in the mesostasis (Fig. 6; Roszjar et al., 2009b). They are typically located interstitial to  
337 ilmenite, pyroxene, plagioclase, and iron metal, and/or occur as inclusions in ilmenite and are  
338 subhedral to anhedral, and rounded in shape. The major element composition is consistent for all  
339 analyzed zircon grains (see Table 2), and within the range of prior published data on eucrite zircon  
340 grains (Saiki et al., 1990; Bukovanská et al., 1991; Ireland and Bukovanská, 1992; Yamaguchi et al.,  
341 2001; Yamaguchi and Misawa 2001; Misawa et al., 2005; Barrat et al., 2007; Roszjar et al., 2009c). In  
342 addition to BSE images that were taken for all selected zircon grains, cathodoluminescence images  
343 were exemplarily taken for some of them. Here it was found that the luminescence behavior is distinct  
344 from grain to grain. Nevertheless, some zircon grains are characterized by partial luminescence with a  
345 preferred direction, increasing towards the edges of the grains, also giving evidence for a thermal  
346 reaction front caused by a metamorphic event (Fig. 6).

#### 347 *Shock features*

348 Northwest Africa 5073 as a whole is very weakly shocked, possibly equivalent to a S2 stage as  
349 defined for chondrites (Stöffler et al., 1991; Bischoff and Stöffler, 1992). Evidence for shock is given  
350 by the undulatory extinction of about half of the plagioclases and the occurrence of dislocation lines in  
351 large pyroxene laths.

352 There is also evidence for an earlier shock event which affected this meteorite prior to annealing  
353 during thermal metamorphism. Minor tiny, euhedral to subhedral troilite (FeS) grains and blebs of  
354 metallic Fe-Ni that are usually  $<3 \mu m$ , occur within the plagioclase crystals and are arranged in  
355 curvilinear trails, frequently aligned in a pearl chain manner, which do not follow the cleavage planes  
356 and are restricted to the interiors of individual silicate crystals. It is known that metal and sulfide are

357 readily mobilized and re-precipitated in the shape of trails during shock metamorphism (Rubin, 1992).  
358 These inclusions are in principle the cause of the silicate darkening which can be described as impact-  
359 generated “shock darkening” (Rubin, 1992; Dodd, 1981). After annealing the metal and sulfide veins  
360 are probably transformed to the tiny blebs described above.

#### 361 *Bulk chemical composition*

362 The major and trace element abundances of NWA 5073 share similarities with other Stannern-  
363 trend eucrites, such as Bouvante and Stannern (Table 3). Northwest Africa 5073 has respectively  
364  $\text{FeO}_{\text{total}}/\text{MgO}$  ratio (2.31) and Sc concentration (25.8  $\mu\text{g/g}$ ) slightly lower, and MgO (8.70 wt%),  $\text{Cr}_2\text{O}_3$   
365 (0.59 wt%) concentrations higher to that of typical Main Group eucrites (e.g., Warren et al., 2009).  
366 Similar “high” MgO abundances were previously measured on Pomozdino by Warren et al. (1990),  
367 and led these authors to propose that this meteorite could be a partial cumulate. Moreover, an increase  
368 of MgO can be produced by a slight oversampling of pyroxene in the powdered sample. Because  
369 NWA 5073 is unequilibrated, these two possibilities can be easily discussed. We have calculated the  
370 apparent distribution coefficient between the pigeonite cores (with  $n = 27$ ) and the whole rock  
371 composition ( $K_D^{\text{Fe/Mg}} = (\text{Fe}/\text{Mg})_{\text{pigeonite core}}/(\text{Fe}/\text{Mg})_{\text{whole rock}}$ ). The result,  $K_D^{\text{Fe/Mg}} = 0.32 \pm 0.01$  ( $2\sigma$ ), is in  
372 very good agreement with experimental distribution coefficients obtained for eucritic systems ( $K_D^{\text{Fe/Mg}}$   
373  $= 0.30$ ; Stolper, 1977). A lower value would have been obtained if the powder contained a pyroxene  
374 excess. Thus, the pigeonite cores formed from a parental melt displaying the same Fe/Mg as the  
375 analyzed powder. We conclude that the whole rock composition is probably close to its parental melt.  
376 However, we suspect that the rather high  $\text{Cr}_2\text{O}_3$  abundance is an artifact produced by a very small  
377 excess of chromite in the powder.

378 Weathered meteorite finds from the Sahara generally exhibit marked Ba and Sr enrichments that are  
379 sensitive indicators for the development of secondary phases (e.g., Stelzner et al., 1999; Barrat et al.,  
380 2003; Crozaz et al., 2003). NWA 5073 is no exception, and displays high Ba and Sr concentrations  
381 (177  $\mu\text{g/g}$  and 2131  $\mu\text{g/g}$ , respectively). It should be noted that its Th/U ratio ( $= 3.38$ ) and Pb  
382 abundances ( $= 0.24 \mu\text{g/g}$ ), which are other possible indicators of weathering, do not show perturbed  
383 values.

384 Although NWA 5073 is characterized by a low FeO/MgO ratio (Fig. 7, Table 3), it displays high  
385 levels of concentrations for incompatible elements, as exemplified by the REEs (Fig. 8). This suggests  
386 that NWA 5073 is a new member of the Stannern-trend eucrites, transitional between the Main Group  
387 and the REE-rich eucrites such as Stannern or Bouvante. Indeed, NWA 5073 exhibits a much more  
388 pronounced negative Eu anomaly ( $\text{Eu}/\text{Eu}^* = 0.68$ ) and a higher Gd/Lu ratio than a regular Main Group  
389 or Nuevo Laredo eucrite, and its REE-pattern is parallel to those of the Stannern-trend eucrites (e.g.,  
390 Bouvante and Stannern). These similarities extend to other incompatible trace element abundances,  
391 and, interestingly, NWA 5073 displays a marked negative Be anomaly (Fig. 9) which is a distinctive  
392 feature of the Stannern-trend eucrites (Barrat et al., 2007). Thus, we can deduce that NWA 5073 is  
393 clearly a new member of this rare group of eucrites.

394 *Mineral chemical composition*

395 In addition to bulk rock trace elements, REE concentrations of pyroxenes and plagioclases  
396 have been determined with LA-ICP-MS. Results are shown in Table 4. CI normalized REE patterns  
397 for pyroxenes and plagioclases are presented in Fig. 10. In eucrites, pyroxene is one of the dominant  
398 phases next to plagioclase, and a sensitive indicator of intrinsic variables such as oxygen fugacity and  
399 temperature that may affect their crystallization sequence. Therefore, major, minor, and trace elements  
400 have been investigated in order to decipher the evolution of the NWA 5073 meteorite. Rare earth  
401 element abundances of selected pyroxene cores in NWA 5073 are in the range of  $0.02\times$  (La) to  $2.2\times$   
402 (Lu) CI chondritic abundances, relative to the values given in Evensen et al. (1978), which is within  
403 the range presented by Pun and Papike (1996). All analyzed pigeonite cores in NWA 5073 exhibit  
404 variable REE abundances that correlate with Ca concentrations, and are generally HREE-enriched  
405 with a pronounced negative Eu anomaly ( $\text{Eu}/\text{Eu}^*=0.68$ ). A total of 7 plagioclase grains have been  
406 analyzed for their REE abundances. The latter exhibit a pronounced positive Eu anomaly with  $\text{Eu}/\text{Eu}^*$   
407 = 61, thus are in agreement with the data range for eucrites previously reported in literature (e.g., Hsu  
408 and Crozaz, 1996; Floss et al., 2000). The REE patterns of single plagioclases are slightly fractionated  
409 with LREE being enriched. The total abundance of REE ranges from  $2\times$  (La) to  $0.1$  (Er)  $\times$  CI  
410 (Evensen et al., 1978), except for Eu (Table 4).

411 *Oxygen isotope composition*

412 The oxygen isotope composition of NWA 5073 obtained in this study ( $\delta^{17}\text{O} = 1.89\text{‰}$ ,  $\delta^{18}\text{O} =$   
413  $4.05\text{‰}$ ,  $\Delta^{17}\text{O} = -0.24\text{‰}$ ) is plotted in Fig. 11 along with the data for other HED samples obtained by  
414 Greenwood et al. (2005). The  $\Delta^{17}\text{O}$  value for NWA 5073 is close to the average HED value of  $-0.239$   
415  $\pm 0.007$  ( $1\sigma$ ) obtained by Greenwood et al. (2005) and indicates that the meteorite is a normal member  
416 of the HED suite (Roszjar et al., 2009a). NWA 5073 was not acid leached prior to oxygen isotope  
417 analysis and has a slightly elevated  $\delta^{18}\text{O}$  value compared to the eucrites analyzed by Greenwood et al.  
418 (2005), which may reflect a small degree of terrestrial weathering. However, the  $\delta^{18}\text{O}$  composition of  
419 NWA 5073 is within the range obtained by Wiechert et al. (2004), which extends to  $\delta^{18}\text{O}$  values of  
420  $4.5\text{‰}$ .

421 *Structural state of zircon grains as obtained by Raman spectroscopy*

422 It has been demonstrated that micro-Raman spectroscopy is a powerful tool to quantify the  
423 degree of self-irradiation damage in single zircon grains caused by the radioactive decay of  
424 incorporated U and Th (metamictization) as well as the structural recovery by thermal annealing  
425 (Nasdala et al., 1995, 1998, 2001; Wopenka et al., 1996; Zhang et al., 2000a- c; Geisler et al., 2001;  
426 Geisler, 2002; Palenik et al., 2003). As already mentioned, the  $\nu_3(\text{SiO}_4)$  band, reflecting antisymmetric  
427 Si-O stretching motions of the  $\text{SiO}_4$  tetrahedra, is particularly sensitive to structural changes associated  
428 with self-irradiation. Raman measurements of zircon grains in sample NWA 5073 reveal a decreased  
429 frequency and an increased broadening of the  $\nu_3(\text{SiO}_4)$  band with increasing radiation dose ( $D$ ; Fig.  
430 12) as calculated from the U and Th concentration measured by EPMA and an inferred age of 4.55 Ga

431 (Table 5). The frequency shift is attributed to an increase in interatomic distances, i.e., to a slight  
432 expansion of the lattice of the crystalline domains, whereas the increase in linewidths is attributed to  
433 the fact that the distribution of bond lengths and bond angles within and between SiO<sub>4</sub> tetrahedra  
434 becomes increasingly irregular (Wopenka et al., 1996).

435 In the diagram linewidth (given as FWHM) vs. frequency of the  $\nu_3(\text{SiO}_4)$  band all measurements plot  
436 along the radiation damage trend (*RDT*; Fig. 13a) that is mainly defined by measurements from  
437 variably self-irradiation-damaged, alluvial zircons from Sri Lanka (Geisler et al., 2001). Dry annealing  
438 experiments with self-irradiation-damaged zircon revealed that episodically annealed samples plot  
439 above the RDT (arrows in Fig. 13a). A comparison of Raman data from natural zircons with  
440 experimental annealing trends thus allows recognizing episodically annealed zircons, provided that  
441 post-annealing radiation damage did not completely obscure the annealing effect, i.e., did not push the  
442 data points back to the RDT in the frequency versus linewidth diagram shown in Fig. 13a. This means  
443 that most likely only relatively recent episodic annealing events are recognizable in this diagram.  
444 However, the observed congruency with the RDT does not imply that the NWA 5073 zircons were not  
445 annealed during their history. In fact, from the diagram linewidth of the  $\nu_3(\text{SiO}_4)$  band vs.  $\alpha$ -decay  
446 dose (*D*; Fig.13b) it can be observed that all analyzed zircon grains from the NWA 5073 eucrite plot  
447 consistently below the so-called damage accumulation curve, defined by Palenik et al. (2003).  
448 Samples that have been neither episodically nor continuously annealed during their geological history  
449 (i.e., that have accumulated the entire damage over their geologic history) should plot, within errors,  
450 onto this accumulation trend. The observation that most of the measurements from zircon grains of  
451 sample NWA 5073 plot significantly below this curve is unambiguous evidence that they were  
452 thermally annealed (Palenik et al., 2003), either continuously for a prolonged period of time or  
453 episodically as a result of a short time heating event. In the latter case, however, the heating event  
454 must have occurred very early in their history.

455

## 456 **Discussion**

457 Most HED meteorites show textural and chemical evidence for extensive thermal annealing  
458 after crystallization such as: Fe-Mg equilibration in pyroxenes, exsolution of Ca-pyroxenes within host  
459 pigeonites, plagioclase and pyroxene clouding, and recrystallization of lithic clasts and clastic matrices  
460 (e.g., Duke and Silver, 1967; Mason et al., 1979; Takeda and Graham, 1991; Metzler et al., 1995;  
461 Yamaguchi et al., 1996; Bogard and Garrison, 2003; Llorca et al., 2009). Moreover, many eucrites  
462 were brecciated and reheated by impacts (e.g., Metzler et al., 1995; Bogard and Garrison, 2003). In the  
463 case of NWA 5073, the thermal history seems to be very complex. In the following, we discuss  
464 possible scenarios to explain both chemical and textural characteristics of this sample.

465

## 466 **Formation of primary phases in a magma chamber and excavation**

467 Since NWA 5073 is a coarse-grained basaltic sample containing large, elongated pyroxene  
468 crystals that preserved their igneous Mg-Fe zoning, we can infer that this sample derived from a  
469 relatively fast cooling magma source. However, due to the texture and the composition of the crystals  
470 (e.g., Al content), the cooling rate must have been slower than 1 °C/hour (Walker et al., 1978; Powell  
471 et al., 1980). Large pyroxene laths might represent an early crystallized phase from a magma that  
472 experienced fast excavation during volcanic eruption. The process of fast excavation is affiliated to  
473 thermal and pressure relief that caused mechanical stress in preexisting pyroxene crystals, probably  
474 leading to fracturing and bending of the crystals. A fast excavation of the magma onto the surface of  
475 the parent body results in quenching of the melt. Thus, this explains the observed skeletal, and  
476 seemingly cotectic crystallisation of silicates (pyroxenes and plagioclases) and other minor phases,  
477 while leaving the large previously crystallized pyroxene crystals relatively unaffected.

478

### 479 **Episode of secondary annealing and rapid cooling**

480 Several mineralogical and chemical observations clearly indicate an episode of thermal  
481 annealing that caused disturbance of the NWA 5073 sample: (1) disturbance of the Lu-Hf system, as  
482 demonstrated by Roszjar and Scherer (2010), (2) Fe-diffusion along cracks and cleavage planes within  
483 the zoned pyroxene crystals (Fig. 3b-d), and (3) recovery of the crystal structure of zircon grains (Fig.  
484 13b). Based on these observations, it is possible to constrain the time-temperature conditions of the  
485 reheating event which is discussed in the following.

486 The observation of Roszjar and Scherer (2010) that about half of the mineral fractions, mainly  
487 pyroxene-rich fractions and the whole rock, form an isochron of  $4.68 \pm 0.14$  ( $2\sigma$ ) Ga, whereas the  
488 other half, e.g., chromite, metal, plagioclase-rich fractions, define a secondary isochron of  $4.31 \pm 0.14$   
489 ( $2\sigma$ ) Ga, is clear evidence that the Lu-Hf system in some minerals was disturbed. Since the time gap  
490 between the primary crystallisation of the eucrite and the event that disturbed the Lu-Hf system is at  
491 least  $\sim 370$  Ma, thermal metamorphism, driven by internal heat on the parent body, can be ruled out as  
492 the cause for the isotope resetting. On the contrary, it is rather likely that the thermal event was short  
493 and intensive. This is supported by the observations that (i) the primary pyroxenes preserved their  
494 initial magmatic Mg-Fe-Ca zoning, (ii) the exsolution lamellae of augite in the host pyroxene grains  
495 are very thin ( $<1\mu\text{m}$ ), (iii) and the mesostasis shows a fine-grained subophitic texture. A short, but  
496 intense heating event more than 300 Ma after the primary crystallization of the eucrite is only  
497 conceivable by a shock-triggered process, e.g., by a superheated impact melt produced by a large  
498 impact. The impact melt could have been injected into neighbouring target rock lithologies, causing a  
499 short thermal pulse followed by fast cooling. Fast cooling is indicated by the absence of  
500 recrystallization textures, which have neither been observed in the coarse mineral grains nor in the  
501 fine-grained mesostasis. As discussed by Yamaguchi and Mikouchi (2005) small fractions of melt can  
502 be formed when a eucrite is heated to a temperature slightly above its solidus of about  $1100^\circ\text{C}$   
503 (Stolper, 1977) for a short period of time. However, a temperature above the solidus would have

504 caused re-melting of mesostasis components, and a depletion of light rare earth elements (LREE) of  
505 the whole rock, which has not been observed (Fig. 8). This suggests that the NWA 5073 sample was in  
506 fact reheated to a certain degree for a short period of time, but most likely not re-melted. The absence  
507 of any evidence for partial re-melting constrains the maximum annealing temperature to about  
508 1100°C.

509 Assuming a maximum reheating temperature of 1100°C and that the reheating process possibly also  
510 triggered Fe-diffusion along cracks and cleavage planes in large pyroxenes (Fig. 3d), the duration of  
511 the heating event can now be estimated from the relation  $L_D = 2\sqrt{Dt}$ , where  $L_D$  is the diffusion length,  
512  $D$  the diffusion coefficient for Fe-diffusion in pyroxene, and  $t$  the diffusion time. From BSE images  
513 (e.g., Fig. 3d), we measured an average diffusion path length,  $L_D$ , of about 25 µm for Fe-diffusion  
514 between the Fe-rich olivine veins into the pyroxene. Using published diffusion coefficients for Fe-Mg  
515 diffusion in pyroxene (Freer, 1981; Cherniak and Dimanov, 2010; Ganguly and Tazzoli, 1994), we  
516 estimated that the heating to a temperature of about ~1100°C could have only lasted for some hours (5  
517 hours at most). This order of magnitude for the duration of the reheating event obtained from this  
518 back-of-the-envelope calculation is also consistent with the observation that the pigeonite pyroxenes  
519 still show chemical zoning, i.e., were not re-equilibrated. It is noted that the order of magnitude of  
520 hours would also hold for slightly longer diffusion lengths and slightly lower temperatures.

521 Probably the most convincing evidence for a secondary heating event is given by the Raman  
522 measurements of ten zircon grains. In the plot of the linewidth of the  $\nu_3(\text{SiO}_4)$  stretching band near  
523 1008  $\text{cm}^{-1}$ , expressed as the full width at half maximum (FWHM), versus the calculated radiation dose  
524 of a single zircon grain ( $D$ ), most analyzed points plot below the radiation damage accumulation curve  
525 (Fig. 13b). We recall that samples that have neither been episodically nor continuously annealed  
526 during their geological history and accumulated the entire structural damage should plot on this curve.  
527 Laboratory dry annealing experiments with radiation-damaged zircon revealed that the temperature  
528 and duration of a thermal event determines the degree of structural recovery that occurs after a certain  
529 degree of structural damage has been accumulated, i.e., during an episodic annealing event (Geisler et  
530 al., 2001; Geisler, 2002). Considering the low U and Th concentrations measured today, the zircons  
531 accumulated only a limited amount of radiation damage during the first 370 Ma after their  
532 crystallisation in the eucrite melt. Experimental work has shown that significant structural recovery of  
533 less self-irradiation-damaged samples within time scales of a few hours only occurs at temperature in  
534 excess of about 900°C (Geisler et al., 2001; Zhang et al., 2000b; Geisler, 2002). It is thus likely that  
535 the actual temperature of the event affecting the NWA 5073 eucrite was between 900 and 1100°C.

536

### 537 **Formation of olivine-rich veins**

538 The occurrence of veins composed of Fe-rich olivine, secondary plagioclase, and small troilite  
539 and chromite grains inside these veins within large pyroxene phenocrysts (Fig. 3) requires careful  
540 consideration, especially as recent papers have suggested that minerals in these veins might have

541 crystallized from fluids or gases during a metasomatic reaction (Barrat et al., 2011). At this point we  
542 would like to make very clear that the authors have rather different views concerning the formation of  
543 the olivine-rich veins within the cores of pyroxene. Thus, we try to unravel the origin of the olivine-  
544 rich veins in NWA 5073, suggesting two valid possible mechanisms of formation that will be  
545 discussed separately in the following paragraphs:

546

547 **(a) Formation of the olivine-rich veins in NWA 5073 by metasomatism**

548 Based on distinct mineralogical features in eucrites, Barrat et al. (2011) defined a three-type  
549 classification scheme for secondary alteration. The first type is characterized by Fe-enrichment along  
550 cracks that cross cut large pyroxene crystals, and by occasional occurrence of Fe-rich olivine in some  
551 fractures (e.g., Pasamonte). The second type reveals involves deposits of Fe-rich olivine (Fa<sub>64-86</sub>) and  
552 minor amounts of troilite inside the cracks as well as the sporadic occurrence of secondary Ca-rich  
553 plagioclase (An<sub>97-98</sub>) associated with Fe-rich olivine (NWA 2061, Y-75011, and Y-82202). The third  
554 type is identifiable by a more frequent occurrence of Ca-rich secondary plagioclase, partial fillings of  
555 cracks or rims of primary plagioclases with small crystals of secondary plagioclase, and Fe-enrichment  
556 of pyroxenes accompanied by significantly decreased Al contents (NWA 049; Barrat et al., 2011).  
557 According to this scheme, NWA 5073 belongs to the second type, as it contains secondary plagioclase  
558 (An<sub>97-100</sub>) associated with Fe-rich olivine veins, typically located at the grain boundaries between  
559 larger primary plagioclase and large pyroxene laths. Based on these observations, Barrat et al. (2011)  
560 proposed that Fe-rich olivine veins may be secondary precipitation products formed by the interaction  
561 between pyroxene crystals and Fe-rich gas or fluid phases that invaded the pyroxene crystals along  
562 fractures and offset planes. The chemical composition of the metasomatic agent is at present not well  
563 constrained but could have been aqueous (Barrat et al., 2011).

564

565 **(b) Formation of the olivine-rich veins in NWA 5073 by incongruent melting**

566 The large pyroxene crystals contain olivine-rich veins that abruptly end at their margins (Fig.  
567 3a-c). The Fe-rich olivine within these veins is accompanied by An-rich plagioclase, and small Cr-rich  
568 oxides (chromites) and troilites. As shown in Fig. 3, all other adjacent silicate phases (small pyroxenes  
569 and large plagioclases) are devoid of these veins. We believe that the chromites may be of genetic  
570 significance, as it is known that the solubility of Cr<sup>3+</sup> in silicate melts is rather high and Cr<sup>3+</sup> is  
571 immobile in hydrous fluids (e.g., Roeder and Reynolds, 1991). Thus, mobilization and precipitation of  
572 small chromite grains in the olivine-rich veins found in NWA 5073 seems to indicate a magmatic  
573 albeit secondary origin. As an alternative to the arguments presented in the previous paragraph, it may  
574 have been that veins of olivine, anorthite, and Cr-rich oxides were formed by incongruent *in-situ*  
575 melting of pyroxene (Fs<sub>34</sub>Wo<sub>2</sub>) at a temperature slightly above the temperature of formation of  
576 primary, Mg-rich pigeonites, i.e. at about 1150°C (Stolper, 1977). This is suggested to have taken  
577 place during a short period of a small temperature excursion in the magma chamber. The process of



578 incongruent melting must have taken place after formation of primary pyroxenes in the magma  
579 chamber, but prior to excavation of the sample. During this peritectic reaction, olivine forms and the  
580 remaining melt crystallizes minor, extremely Ca-rich plagioclase. A similar process of incongruent  
581 melting of pigeonites producing olivine (Fo<sub>35-55</sub>) plus silica was experimentally shown by e.g.,  
582 Huebner et al. (1973) and Huebner and Turnock (1980). It should be noted that the experimental data  
583 confirm that the olivines in the veins (Fa<sub>65-71</sub>) are in equilibrium with the outer rims of large pyroxene  
584 grains and the small pyroxenes (~Fs<sub>62-68</sub>; Table 2). Since the pyroxene, which melts incongruently,  
585 does not contain significant Na, the crystallizing plagioclase has to be low in Na and, consequently,  
586 extremely rich in Ca (An<sub>97-100</sub>). Cr- and S-rich oxides that are found within the olivine-rich veins are  
587 sometimes also located within the primary pyroxenes. The incongruent melting of pigeonite requires  
588 only a few tens of degrees above the peritectic temperature, so that if we employ the aforementioned  
589 experimental data we estimate some 1150°C for the formation of the olivine veins in this scenario.

590

591 In summary, it seems that both interpretations for the formation of olivine-rich veins in large  
592 pyroxenes, as discussed above, have some inconsistencies which cannot be resolved at this point. The  
593 metasomatism model cannot fully explain the occurrence of Fe-rich olivine veins in large pyroxene  
594 phenocrysts, while the adjacent silicate phases (small pyroxenes and large plagioclases) are devoid of  
595 them. Furthermore, the occurrence of chromite within these veins is hardly explained by metasomatic  
596 fluids. On the other hand, the model which involves incongruent melting cannot readily explain certain  
597 textural observations, such as the only minor occurrence of olivine-rich veins in contact with  
598 plagioclase. To unravel the process which leads to the formation of such Fe-rich olivine veins in large  
599 pyroxenes, one would need further oxygen isotope data of these veins. Furthermore, more realistic  
600 melting experiments on bulk eucrite samples and pyroxenes would be helpful.

601

#### 602 **Pairing or launch-pairing of some Stannern-trend eucrites?**

603 According to sample textures, grain sizes, including the occurrence of Fe-rich olivine veins in  
604 large pyroxenes and secondary plagioclases, NWA 5073 resembles some other Stannern-trend eucrite  
605 finds from the Sahara, namely NWA 1000 and NWA 2061. Since the occurrence of Fe-rich olivine  
606 veins in large pyroxene crystals is not restricted to the NWA 5073 sample, but was also found to occur  
607 in other eucrites and howardites, namely Y-7308, Y-790260, Y-75011, and NWA 1000, Macibini, and  
608 NWA 2061 (Takeda and Yanai, 1982; Takeda et al., 1983; Metzler, 1985; Warren, 2002; Barrat et al.,  
609 2007; and Barrat, unpublished data), one can argue that these findings give some evidence for a large-  
610 scale but certainly not global parent body process. However, NWA 1000 is severely shocked (S4), as  
611 documented by the transformation of half of the plagioclase into maskelynite (Warren, 2002). Thus,  
612 NWA 5073 and NWA 1000 are certainly not fall-paired. Since NWA 2061 is as REE-rich as Stannern  
613 and thus distinct to NWA 5073, a pairing between those eucrites and NWA 5073 seems unlikely.  
614 However a certain pairing, especially for the Stannern-trend eucrite finds with the NWA 5073 sample,

615 can only be unequivocally proven by obtaining noble gas exposure ages. However, some of these  
616 samples may be launch-paired.

617

## 618 **Summary and Conclusions**

619 In summary, our results are: (i) Northwest Africa 5073 is a coarse-grained basaltic,  
620 unequilibrated, and non-brecciated eucrite with a subophitic to slightly variolitic (fan-spherulitic)  
621 texture, mainly composed of small equilibrated pyroxenes (~40 vol.%), elongated, unequilibrated  
622 pyroxene phenocrysts up to 1.2 cm (~ 25 vol.%), plagioclase laths up to 0.3 cm in apparent length  
623 (~26 vol. %), and about 8.5 vol.% mesostasis. (ii) This sample is very weakly shocked and moderately  
624 weathered (W2-3). (iii) Based on its oxygen isotope composition ( $\delta^{17}\text{O} = 1.88 \text{ ‰}$ ,  $\delta^{18}\text{O} = 4.05 \text{ ‰}$ ,  
625  $\Delta^{17}\text{O} = -0.239 \text{ ‰}$ ), we can deduce that NWA 5073 is a normal member of the HED suite of  
626 achondrites. (iv) The large unequilibrated pyroxenes preserved their initial magmatic Mg-Fe-Ca  
627 zoning and are crosscut by olivine-rich veins ( $\text{Fa}_{65-71}$ ) which are restricted to them. These veins also  
628 contain minor chromite, troilite, and very Ca-rich plagioclase. (v) Three different plagioclase  
629 generations occur: (a) large primary plagioclases crystals ( $\text{An}_{76-92}\text{Ab}_{8-22}\text{Or}_{0-3}$ ), (b) small primary  
630 plagioclase grains of similar composition as the large ones that are concentrated in mesostasis areas  
631 and, (c) a secondary generation of small plagioclases ( $\text{An}_{97-100}$ ), typically 5-20  $\mu\text{m}$  in diameter, always  
632 found in association with Fe-rich olivine veins. (vi) Due to the occurrence of these olivine-rich veins  
633 in large pyroxene crystals and the sporadic occurrence of secondary plagioclase associated with the  
634 former, NWA 5073 belongs to stage 2-type eucrites, according to the classification scheme for  
635 secondary alteration as proposed by Barrat et al. (2011). Other members of this group include NWA  
636 2061, Y-75001, Y-82202, and probably NWA 1000 (Barrat et al., 2011). (vii) Based on its bulk  
637 chemical composition (e.g., high Ti with  $\text{TiO}_2 = 0.77 \text{ wt.}\%$ ,  $\text{La} = 4.18 \text{ }\mu\text{g/g}$ , negative Be anomaly),  
638 NWA 5073 displays a distinctive Stannern-trend signature. (viii) The REE pattern of NWA 5073 bulk  
639 rock, which is characterized by flat LREE and a slight HREE-depletion ( $\text{La}_n/\text{Yb}_n=1.38$ ) with a  
640 pronounced negative Eu anomaly ( $\text{Eu}/\text{Eu}^*=0.68$ ), resembles those of other Stannern-trend eucrites.  
641 (ix) Northwest Africa 5073 contains zircon grains up to 30  $\mu\text{m}$  in size that were invariably found in  
642 the mesostasis. These zircon grains are metamict and were annealed, indicating a short high-  
643 temperature event (probably induced by shock) occurring after primary crystallization of main sample  
644 constituents. (x) A short but intense heating event that caused disturbance of the sample is also  
645 indicated by the disturbance of the Lu-Hf system, and Fe-diffusion along cracks and cleavage planes  
646 within unequilibrated pyroxene crystals. (xi) According to sample textures, grain sizes, and the degree  
647 of alteration, including the occurrence of olivine-rich veins in large pyroxenes, as well as secondary  
648 plagioclases, NWA 5073 resembles some other Stannern-trend eucrite finds from the Sahara, namely  
649 NWA 1000, NWA 2061 and NWA 4523. However, these four samples are unlikely fall-paired as  
650 discussed above.

651

652 **Acknowledgements**

653 The authors are grateful to A. Yamaguchi and an anonymous reviewer for their helpful reviews, which  
654 helped improving the paper and A. Ruzicka for thoughtful comments and for handling this article. We  
655 also thank U. Heitmann for sample preparation, C. Bollinger for assistance at the LA-ICP-MS, J.  
656 Berndt for guidance with the electron microprobe, and M. Menneken for help with Raman  
657 measurements. This study was partially supported by the German Research Foundation (DFG; grant  
658 Bi 344/9-1) and T. Geisler acknowledges a Heisenberg scholarship from the DFG.

659

660 **References**

- 661 Åmli R. and Griffin W. L. 1975. Microprobe analysis of REE minerals using empirical correction  
662 factors. *American Mineralogist* 60:599-606.  
663
- 664 Armstrong J. T. 1991. Quantitative elemental analysis of individual microparticles with electron beam  
665 instruments. *Electron Probe Quantitation*, edited by Heinrich K. F. J. and Newbury D. E. New  
666 York: Plenum Press. pp. 261-315.  
667
- 668 Barrat J. A., Blichert-Toft J., Gillet Ph. and Keller F. 2000. The differentiation of eucrites: the role of  
669 in-situ crystallization. *Meteoritics & Planetary Science* 35:1087-1100.  
670
- 671 Barrat J. A., Jambon A., Bohn M., Blichert-Toft J., Sautter V., Göpel C., Gillet Ph., Boudouma O. and  
672 Keller F. 2003. Petrology and geochemistry of the unbrecciated achondrite North West Africa  
673 1240 (NWA 1240): an HED parent body impact melt. *Geochimica et Cosmochimica Acta* 67:3959-  
674 3970.  
675
- 676 Barrat J. A., Yamaguchi A., Greenwood R. C., Bohn M., Cotten J., Benoit M., and Franchi I. A. 2007.  
677 The Stannern trend eucrites: contamination of main group eucritic magmas by crustal partial melts.  
678 *Geochimica et Cosmochimica Acta* 71:4108-4124.  
679
- 680 Barrat J. A., Yamaguchi A., Benoit M., Cotten J. and Bohn M. 2008. Geochemistry of diogenites: Still  
681 more 392 diversity in their parental melts. *Meteoritics & Planetary Science* 43:1759-1775.  
682
- 683 Barrat J. A., Yamaguchi A., Greenwood R. C., Bollinger C., Bohn M., and Franchi I. A. 2009. Trace  
684 element geochemistry of K-rich impact spherules from howardites. *Geochimica et Cosmochimica*  
685 *Acta* 73:5944-5958.  
686
- 687 Barrat J.A., Yamaguchi A., Zanda B., Bollinger C., Bohn M. (2010) Relative chronology of crust  
688 formation on asteroid 4-Vesta: Insights from the geochemistry of diogenites. *Geochimica et*  
689 *Cosmochimica Acta* 74:6218-6231.  
690
- 691 Barrat J. A., Yamaguchi A., Bunch T. E., Bohn M., Bollinger C., and Ceuleneer G. 2011. Possible  
692 fluid-rock interactions on differentiated asteroids recorded in eucrite eucritic meteorites.  
693 *Geochimica et Cosmochimica Acta* 75:3839-3852.  
694
- 695 Beck A. W. and McSween H. Y. Jr. 2010. Diogenites as polymict breccias composed of  
696 orthopyroxenite and harzburgite. *Meteoritics & Planetary Science* 45:850-872.  
697
- 698 Binzel R. P. and Xu S. 1993. Chips off of Asteroid 4 Vesta: Evidence for the parent body of basaltic  
699 achondrite meteorites. *Science* 260:186-191.  
700
- 701 Bischoff A. and Stöffler D. 1992. Shock metamorphism as a fundamental process in the evolution of  
702 planetary bodies: Information from meteorites. *European Journal of Mineralogy* 4:707-755.

703  
704 Bischoff A., Scott E. R. D., Metzler K., and Goodrich C. A. 2006. Nature and origins of meteoritic  
705 breccias. *Meteorites and the early solar system II*, edited by Lauretta D.S. and McSween H.Y.  
706 Tucson: The University of Arizona Press. pp 679-712.  
707  
708 Bland P. A., Spurný P., Towner M. C., Bevan A. W. R., Singleton A. T., Bottke W.F. Jr., Greenwood  
709 R. C., Chesley S. R., Shrubený L., Borovička J., Ceplecha Z., McClafferty T. P., Vaughan D.,  
710 Benedix G. K., Deacon G., Howard K. T., Franchi I. A., Hough R. M. 2009. An anomalous basaltic  
711 meteorite from the innermost main belt. *Science* 325:1525-1527.  
712  
713 Bogard D. and Garrison D. 2003.  $^{39}\text{Ar}$ - $^{40}\text{Ar}$  ages of eucrites and thermal history of asteroid 4 Vesta.  
714 *Meteoritics & Planetary Science* 38:669-710.  
715  
716 Bukovanská M., Ireland T. R., El Goresy A., Palme H., Spettel B., and Wlotzka F. 1991. Zircons in  
717 the Padvarnikai brecciated eucrite (abstract). *Meteoritics* 26:325.  
718  
719 Cherniak D. J. and Dimanov A. 2010. Diffusion in pyroxene, mica and amphibole. *Reviews in*  
720 *Mineralogy & Geochemistry* 72:641-690.  
721  
722 Consolmagno G. J. and Drake M. J. 1977. Composition and evolution of the eucrite parent body:  
723 Evidence from rare earth elements. *Geochimica et Cosmochimica Acta* 41:1271-1282.  
724  
725 Cotten J., Ledez A., Bau M., Caroff M., Maury R. C., Dulski P., Fourcade S., Bohn M., and Brousse  
726 R. 1995. Origin of anomalous Rare-Earth Element and Yttrium enrichments in subaerially exposed  
727 basalts - Evidence from French-Polynesia. *Chemical Geology* 119:115-138.  
728  
729 Crozaz G., Floss C. and Wadhwa M. 2003. Chemical alteration and REE mobilization in meteorites  
730 from hot and cold deserts. *Geochimica et Cosmochimica Acta* 67:4727-4741.  
731  
732 Dawson P., Hargreave M. M., and Wilkinson G. R. 1971. The vibrational spectrum of zircon ( $\text{ZrSiO}_4$ ).  
733 *Journal of Physics C: Solid State Physics* 4:240-256.  
734  
735 Dodd R. T. 1981. Meteorites- A Petrologic-Chemical Synthesis. *Cambridge University Press, New*  
736 *York, New York, USA, 368 p.*  
737  
738 Drake M.J. 2001. The eucrite/Vesta story. *Meteoritics & Planetary Science* 36:501-513.  
739  
740 Duke M. B., and Silver L. T. 1967. Petrology of eucrites, howardites and mesosiderites. *Geochimica et*  
741 *Cosmochimica Acta* 31:1637-1665.  
742  
743 Evensen N. M., Hamilton P. J., and O'Nions R. K. 1978. Rare Earth abundances in chondritic  
744 meteorites. *Geochimica et Cosmochimica Acta* 42:1199-1212.  
745  
746 Floss C., Crozaz G., Yamaguchi A., and Keil K. 2000. Trace element constraints on the origins of  
747 highly metamorphosed Antarctic eucrites. *Antarctic Meteorite Research* 13:222-237.  
748  
749 Freer R. 1981. Diffusion in Silicate Minerals and Glasses: A Data Digest and Guide to the Literature.  
750 *Contributions to Mineralogy and Petrology* 76:440-454.  
751  
752 Ganguly J. and Tazzoli V. 1994.  $\text{Fe}^{2+}$ -Mg interdiffusion in orthopyroxene: Retrieval from the data on  
753 intracrystalline exchange reaction. *American Mineralogist* 79:930-937.  
754  
755 Geisler T. 2002. Isothermal annealing of partially metamict zircon: evidence for a three-stage recovery  
756 process. *Physics and Chemistry of Minerals*. 29:420-429.  
757

758 Geisler T., Pidgeon R. T., van Bronswijk W., and Pleysier R. 2001. Kinetics of thermal recovery and  
759 recrystallization of partially metamict zircon: a Raman spectroscopic study. *European Journal of*  
760 *Mineralogy* 13:1163-1176.  
761

762 Gounelle M., Chaussidon M., Morbidelli A., Barrat J. A., Engrand C., Zolensky M. E. and McKeegan  
763 K. D. 2009. A unique basaltic micrometeorite expands the inventory of solar system planetary  
764 crusts. *Proceedings of the National Academy of Sciences of the United States of America* 106:6904-  
765 6909.  
766

767 Greenwood R. C., Franchi I. A., Jambon A., and Buchanan P. C. 2005. Widespread magma oceans on  
768 asteroidal bodies in the early Solar System. *Nature* 435:916-918.  
769

770 Harlow G. E. and Klimentidis R. 1980. Clouding of pyroxene and plagioclase in eucrites: implications  
771 for post-crystallization processing. *Proceedings, 11th Lunar Science Conference*. pp. 1131-1148.  
772

773 Hoskin P. W. O. and Rodgers K. A. 1996. Raman spectral shift in the isomorphous series  $(Zr_{1-x}Hf_x)SiO_4$ . *European Journal of Solid State Inorganic Chemistry* 33:1111-1121.  
774  
775

776 Huebner J. S. and Turnock A. C. 1980. The melting relations at 1bar of pyroxenes composed largely  
777 of Ca-, Mg-, and Fe-bearing components. *American Mineralogist* 65:225-271.  
778

779 Huebner J. S., Ross M., Hickling N. 1973. Partial melting of pyroxenes and the origin of mare basalts  
780 (abstract), *Lunar and Planetary Conference* 4:397-399.  
781

782 Hsu W. and Crozaz G. 1996. Mineral chemistry and the petrogenesis of eucrites: I. Noncumulate  
783 eucrites. *Geochimica et Cosmochimica Acta* 60:4571-4591.  
784

785 Ireland T. R. and Bukovanskà M. 1992. Zircons from the Stannern eucrite (abstract). *Meteoritics*  
786 27:237.  
787

788 Jochum K. P., Willbold M., Raczeck I., Stoll B., and Herwig K. 2005. Chemical characterisation of  
789 the USGS reference glasses GSA-1G, GSC-1G, GSD-1G, GSE-1G, BCR2-G, BHVO2-G, and  
790 BIR1-G using EPMA, ID-TIMS, ID-ICP-MS and LA-ICP-MS. *Geostandards and Geoanalytical*  
791 *Research* 29:285-302.  
792

793 Llorca J., Casanova I., Trigo-Rodriguez J. M., Madeido J. M., Roszjar J., Bischoff A., Ott U., Franchi  
794 I. A., Greenwood R. C., and Laubenstein M. 2009. The Puerte Lápice eucrite. *Meteoritics &*  
795 *Planetary Science* 44:159-174.  
796

797 Mason B., Jarosewich E., and Nelen J. A. 1979. The pyroxene-plagioclase achondrites. *Smithsonian*  
798 *Contributions to the Earth Sciences* 22:27-45.  
799

800 Mayne R. G., McSween H. Y., Jr., McCoy T. J., Gale A. 2009. Petrology of the unbrecciated eucrites.  
801 *Geochimica et Cosmochimica Acta* 73:794-819.  
802

803 McCord T. B., Adams J. B., and Johnson T.V. 1970. Asteroid Vesta: Spectral reflectivity and  
804 compositional implications. *Science* 168:1445-1447.  
805

806 McSween H. Y. Jr., Mittlefehldt D. W., Beck A. B., Mayne R. G., McCoy T. J. 2010. HED Meteorites  
807 and their relationship to the geology of Vesta and Dawn mission. *Space Science Reviews*. 34p.  
808

809 Metzler, K. 1985. Gefüge und Zusammensetzung von Gesteinsfragmenten in polymikten  
810 achondritischen Breccien. *Diploma thesis*, University of Münster, 150 pp.  
811

812 Metzler K., Bobe K. D., Palme H., Spettel B., and Stöffler D. 1995. Thermal and impact  
813 metamorphism on the HED parent asteroid. *Planetary and Space Science* 43:499-525.

814  
815 Miller M. F. 2002. Isotopic fractionation and the quantification of  $^{17}\text{O}$  anomalies in the oxygen three-  
816 isotope system: an appraisal and geochemical significance. *Geochimica et Cosmochimica Acta*  
817 66:1881-1889.  
818  
819 Miller M. F., Franchi I. A., Sexton A. S., and Pillinger C. T. 1999. High precision  $\delta^{17}\text{O}$  isotope  
820 measurements of oxygen from silicates and other oxides: Method and Applications. *Rapid*  
821 *Communications in Mass Spectrometry* 13:1211-1217.  
822  
823 Misawa K., Yamaguchi A., and Kaiden H. 2005. U-Pb and  $^{207}\text{Pb}$ - $^{206}\text{Pb}$  ages of zircons from basaltic  
824 eucrites: Implications for early basaltic volcanism on the eucrite parent body. *Geochimica et*  
825 *Cosmochimica Acta* 69:5847-5861.  
826  
827 Mittlefehldt D. W. 2000. Petrology and geochemistry of the Elephant Moraine A79002 diogenite: A  
828 genomict breccia containing a magnesian harzburgite component. *Meteoritics & Planetary Science*  
829 35:901-912.  
830  
831 Mittlefehldt D. W. and Lindstrom M. M. 2003. Geochemistry of eucrites: genesis of basaltic eucrites,  
832 and Hf and Ta as petrogenetic indicators for altered Antarctic eucrites. *Geochimica et*  
833 *Cosmochimica Acta* 67:1911-1935.  
834  
835 Mittlefehldt D. W., McCoy T. J., Goodrich C. A., and Kracher A. 1998. Non-chondritic meteorites  
836 from asteroidal bodies. In *Reviews in Mineralogy*, edited by Papike J. J., vol 36. Washington D. C.:  
837 Mineralogical Society of America. pp. 4-1-4-195.  
838  
839 Nasdala L., Irmer G., and Wolf D. 1995. The degree of metamictization in zircon: a Raman  
840 spectroscopic study. *European Journal of Mineralogy* 7:471-478.  
841  
842 Nasdala L., Pidgeon R. T., Wolf D. 1996. Heterogeneous metamictization of zircon on a microscale,  
843 *Geochimica et Cosmochimica Acta* 60:1091-1097.  
844  
845 Nasdala L., Götze J., Pidgeon R. T., Kempe U., and Seifert T. 1998. Constraining a SHRIMP U-Pb  
846 age: microscale characterization of zircons from Saxionian Rotliegende rhyolites. *Contributions to*  
847 *Mineralogy and Petrology* 132:300-306.  
848  
849 Nasdala L., Wenzel M., Varva G., Irmer G., Wenzel T., and Kober B. 2001. Metamictisation of  
850 natural zircon: accumulation versus thermal annealing of radioactivity-induced damage.  
851 *Contributions to Mineralogy and Petrology* 141:125-144.  
852  
853 Nasdala L., Reiners P.W., Garver J.I., Kennedy A.K., Stern R.A., Balan E., and Wirth R. (2004)  
854 Incomplete retention of radiation damage in zircon from Sri Lanka. *American Mineralogist* 89:  
855 219-231.  
856  
857 Palenik C. S., Nasdala L., and Ewing R. C. 2003. Radiation damage in zircon. *American Mineralogist*  
858 88:777-781.  
859  
860 Powell M. A., Walker D., and Hays J. F. 1980. Experimental solidification of a eucrite basalt:  
861 Microprobe studies (abstract). *Lunar and Planetary Science* 11:896-898.  
862  
863 Pun A. and Papike J. J. 1996. Unequilibrated eucrites and the equilibrated Juvinas eucrite: Pyroxene  
864 REE systematics and major, minor, and trace element zoning. *American Mineralogist* 81:1438-  
865 1451.  
866  
867 Righter K. and Drake M. J. 1997. A magma ocean on Vesta: core formation and petrogenesis of  
868 eucrites and 471 diogenites. *Meteoritics & Planetary Science* 32:929-944.  
869

870 Roeder P. L. and Reynolds I. 1991. Crystallization of chromite and chromium solubility in basaltic  
871 melts. *Journal of Petrology* 32:909-934.  
872

873 Roszjar J., Metzler K., Bischoff a., Greenwood R. C., and Franchi I. A. 2009a. Northwest Africa  
874 (NWA) 5073 - An eucritic basalt with cm-sized pyroxenes (abstract). *Meteoritics & Planetary  
875 Science* 44:5202.  
876

877 Roszjar J., Geisler T., Scherer E. E., and Bischoff A. 2009b. The thermal history of zircon from the  
878 NWA5073 eucrite as revealed by Raman spectroscopy (abstract). *Meteoritics & Planetary Science*  
879 44:5203.  
880

881 Roszjar J., Srinivasan G., Bischoff A., Mezger K., and Whitehouse M. 2009c. Hf-W ages of zircons -  
882 New constraints on the evolution of the eucrite parent body (abstract #1655), 40th *Lunar and  
883 Planetary Science Conference*.  
884

885 Roszjar J. and Scherer E. E. 2010. Lu-Hf systematics of the NWA 5073 eucrite reflect a complex  
886 thermal history (abstract). *Meteoritics & Planetary Science* 45:5425.  
887

888 Rubin A. E. 1992. A shock-metamorphic model for silicate darkening and compositionally variable  
889 plagioclase in CK and ordinary chondrites. *Geochimica et Cosmochimica Acta* 56:1705-1714.  
890

891 Ruzicka A., Snyder G. A. and Taylor L. A. 1997. Vesta as the howardite, eucrite and diogenite parent  
892 body: 477 implications for the size of a core and for large-scale differentiation. *Meteoritics &  
893 Planetary Science* 32:825-840.  
894

895 Saiki K., Takeda H., and Tabei T. 1990. Zircon in magnesian, basaltic eucrite Yamato 791438 and its  
896 Possible Origin (abstract). *Lunar and Planetary Science* 21:341-349.  
897

898 Scott E. R. D., Greenwood R. C., Franchi I. A. and Sanders I. S. 2009. Oxygen isotopic constraints on  
899 the origin 489 and parent bodies of eucrites, diogenites, and howardites. *Geochimica et  
900 Cosmochimica Acta* 73: 5835-5853.  
901

902 Stelzner T., Heide K., Bischoff A., Weber A., Weber D., Scherer P., Schukz L., Happel M., Schrön  
903 W., Neupert U., Michel R., Clayton R. N., Mayeda T. K., Bonani G., Haidas I., Ivy-Ochs S., and  
904 Suter M. 1999. In interdisciplinary study of weathering effects in ordinary chondrites from the  
905 Acfer region Algeria, *Meteoritics & Planetary Science* 34:787-794.  
906

907 Stolper E. 1977. Experimental petrology of eucritic meteorites. *Geochimica et Cosmochimica Acta*  
908 41:587-611.  
909

910 Stöffler D., Bischoff A., Buchwald V., and Rubin A. E. 1988. Shock effects in meteorites. In  
911 *Meteorites and the Early Solar System*, edited by Kerridge J. F. and Matthews J. F., Tucson:  
912 University of Arizona Press, pp. 165-202.  
913

914 Stöffler D., Keil K., and Scott E. R. D. 1991. Shock metamorphism of ordinary chondrites.  
915 *Geochimica et Cosmochimica Acta* 55:3845-3867.  
916

917 Takeda H. 1979. A layered-crust model of a howardite parent body. *Icarus* 40:455-470.  
918

919 Takeda H. 1991. Comparison of Antarctic and non-Antarctic achondrites and possible origin of the  
920 differences. *Geochimica et Cosmochimica Acta* 55:35-47.  
921

922 Takeda H., and Yanai K. 1982. Mineralogical examination of the Yamato 79 achondrites: polymict  
923 eucrites and ureilites. Proceedings 7th Symposium on Antarctic meteorites. pp. 97-123.  
924

- 925 Takeda H. and Graham A. L. 1991. Degree of equilibrium of eucritic pyroxenes and thermal  
926 metamorphism of the earliest planetary crust. *Meteoritics* 26:129-134.  
927
- 928 Takeda H., Mori H., Yanai K., and Wooden J. L. 1982. Three different basalt types in Antarctic  
929 polymict eucrites, a view from pyroxene chemical zoning trend (abstract), *Lunar and Planetary  
930 Science* 13:792-293.  
931
- 932 Takeda H., Mori H., Delaney J. S., Prinz M., Harlow G. E., and Ishii T. 1983. Mineralogical  
933 comparison of antarctic and non-antarctic HED (howardites-eucrites-diogenites) achondrites.  
934 Proceedings, 8th Symposium on Antarctic Meteorites. pp. 181-205.  
935
- 936 Takeda H., Mori H., and Bogard D. D. 1994. Mineralogy and  $^{39}\text{Ar}$ - $^{40}\text{Ar}$  age of an old pristine basalt:  
937 Thermal history of the HED parent body. *Earth and Planetary Science Letters* 122:183-194  
938
- 939 Tanabe K. and Hiraishi J. 1980. Correction of finite slit width effects on Raman line widths.  
940 *Spectrochimica Acta Part A: Molecular Spectroscopy* 36:341-344.  
941
- 942 Walker D., Powell M. A., Lofgren G. E., and Hays J. F. 1978. Dynamic crystallization of a eucritic  
943 basalt. Proceedings, 9th *Lunar and Planetary Science Conference*. pp. 1369-1391.  
944
- 945 Warren P. H. 1997. Magnesium oxide-iron oxide mass balance constraints and a more detailed model  
946 for the 502 relationship between eucrites and diogenites *Meteoritics & Planetary Science* 32:945-  
947 963.  
948
- 949 Warren P. H. 2002. Northwest Africa 1000: A new eucrite with maskelynite, unequilibrated pyroxene  
950 crisscrossed by fayalite-rich veins, and Stannern-like geochemistry (abstract #1147). 33rd *Lunar  
951 and Planetary Science Conference*.  
952
- 953 Warren P. H. and Jerde E. 1987. Composition and origin of Nuevo Laredo trend eucrites. *Geochimica  
954 et Cosmochimica Acta* 51:713-725.  
955
- 956 Warren P. H. and Kallemeyn G. W. 2001. Eucrite Bluewing 001: a Stannern-like bulk composition  
957 and its linkage with other unequilibrated HED basalts (abstract). *Lunar and Planetary Science*  
958 32:2114.  
959
- 960 Warren P. H., Jerde E. A., Migdisova L. F., Yaroshevsky A. A. 1990. Pomozdino: An anomalous,  
961 high-MgO/FeO, yet REE-rich eucrite, Proceedings, 20th Lunar and Planetary Science Conference.  
962 pp. 281-297.  
963
- 964 Warren P. H., Kallemeyn G. W., Huber H., Ulf-Møller F., and Choe W. 2009. Siderophile and other  
965 geochemical constraints on mixing relationships among HED-meteorite breccias. *Geochimica et  
966 Cosmochimica Acta* 73:5918-5943.  
967
- 968 Wiechert U. H., Halliday A. N., Palme H., and Rumble D. 2004. Oxygen isotope evidence for rapid  
969 mixing of the HED parent body. *Earth and Planetary Science Letters* 221:373-382.  
970
- 971 Wlotzka F. 1993. A weathering scale for the ordinary chondrites (abstract). *Meteoritics* 28:460.  
972
- 973 Wopenka B., Jolliff B. L., Zinner E., and Kremser R. 1996. Trace element zoning and incipient  
974 metamictization in a lunar zircon: Application of three microprobe techniques. *American  
975 Mineralogist* 81:902-912.  
976
- 977 Yamaguchi A. and Mikouchi T. 2005. Heating experiments of the HaH 262 eucrite and implication for  
978 the metamorphic history of highly metamorphosed eucrites (abstract). *Lunar and Planetary Science*  
979 36: 1574 (CD).  
980



981 Yamaguchi A. and Misawa K. 2001. Occurrence and possible origin of zircon in basaltic eucrites  
982 (abstract). *Antarctic Meteorites* 26:165-166.  
983  
984 Yamaguchi A., Taylor G. J., and Keil K. 1996. Global metamorphism on the eucrite parent body.  
985 *Icarus* 124:97-112.  
986  
987 Yamaguchi A., Taylor G. J., Keil K., Floss C., Crozaz G., Nyquist L. E., Bogard D. D., Garrison D.  
988 H., Wiesmann H., and Shih C.-Y. 2001. Post-crystallization reheating and partial melting of eucrite  
989 EET90020 by impact into the hot crust of asteroid 4 Vesta ~4.50 Ga ago. *Geochimica et*  
990 *Cosmochimica Acta* 65:3577-3599.  
991  
992 Yamaguchi A., Clayton R. N., Mayeda T. K., Ebihara M., Oura Y., Miura Y. N., Haramura H.,  
993 Misawa K., Kojima H. and Nagao K. 2002. A new source of basaltic meteorites inferred from  
994 Northwest Africa 011. *Science* 296:334-336.  
995  
996 Yamaguchi A., Barrat J. A., Greenwood R. C., Shirai N., Okamoto C., Setoyanagi T., Ebihara M.,  
997 Franchi I. A., and Bohn M. 2009. Crustal partial melting on Vesta: Evidence from highly  
998 metamorphosed eucrites. *Geochimica et Cosmochimica Acta* 73:7162-7182.  
999  
1000 Zhang M., Salje E. K. H., Farnan I., Graeme-Barber A., Daniel P., Ewing R. C., Clark A. M., Rios S.,  
1001 and Leroux H. 2000a. Metamictization of zircon: Raman spectroscopic study. *Journal of Physics:*  
1002 *Condensed Matter* 12:97-112.  
1003  
1004 Zhang M., Salje E. K. H., Farnan I., Capitani G. C., Leroux H., Clark A. M., Schlüter J., and Ewing R.  
1005 C. 2000b. Annealing of  $\alpha$ -decay damage in zircon: a Raman spectroscopic study. *Journal of*  
1006 *Physics: Condensed Matter* 12:3131-3148.  
1007  
1008 Zhang M., Salje E. K. H., Ewing R. C., Farnan I., Rios S., Schlüter J., and Leggo P. 2000c. Alpha-  
1009 decay damage and recrystallization in zircon: evidence for an intermediate state from infrared  
1010 spectroscopy. *Journal of Physics: Condensed Matter* 12:5189-5199.  
1011  
1012  
1013  
1014  
1015  
1016

Table 1. Modal abundance of major phases  
and mesostasis in NWA 5073 (vol.%).

Pyroxene phenocrysts	24.8
Primary feldspars (plagioclases)	26.4
Small pyroxenes	39.9
Mesostasis	8.5
Metal	0.4

Table 2. Chemical composition of mineral phases in NWA 5073. Results in wt.%.

---

	SiO <sub>2</sub>	TiO <sub>2</sub>	Al <sub>2</sub> O <sub>3</sub>	Cr <sub>2</sub> O <sub>3</sub>	FeO*	MnO	MgO	CaO	Na <sub>2</sub> O	K <sub>2</sub> O	P <sub>2</sub> O <sub>5</sub>	HfO <sub>2</sub>	ZrO <sub>2</sub>	Y <sub>2</sub> O <sub>3</sub>	Total	Endmembers average	Endmembers min. – max.	
<b>Major phases</b>																		
Pyroxene cores (n=27)	52.4	0.11	1.11	1.01	18.0	0.62	24.3	1.85	0.02	<0.01	n.d.	n.d.	n.d.	n.d.	99.41	En <sub>55.1</sub> Wo <sub>4.2</sub> Fs <sub>40.7</sub>	En <sub>51.0-60.0</sub> Wo <sub>1.7-7.6</sub> Fs <sub>34.0-45.0</sub>	
Pyroxene rims (n=27)	49.6	0.34	1.11	0.57	25.9	1.04	12.9	8.2	0.03	<0.01	n.d.	n.d.	n.d.	n.d.	99.68	En <sub>27.5</sub> Wo <sub>17.4</sub> Fs <sub>55.1</sub>	En <sub>19.8-34.1</sub> Wo <sub>8.2-33.8</sub> Fs <sub>42.2-62.4</sub>	
Small pyroxenes (n=11)	49.5	0.24	1.07	0.63	29.4	1.17	12.5	5.5	0.02	<0.01	n.d.	n.d.	n.d.	n.d.	100.01	En <sub>26.4</sub> Wo <sub>11.6</sub> Fs <sub>62.0</sub>	En <sub>22.8-35.8</sub> Wo <sub>5.9-18.8</sub> Fs <sub>58.3-68.8</sub>	
Pyroxenes mesostasis (n=5)	49.8	0.42	0.73	0.23	19.2	0.68	9.3	19.7	0.04	0.02	n.d.	n.d.	n.d.	n.d.	100.15	En <sub>27.1</sub> Wo <sub>41.4</sub> Fs <sub>31.5</sub>	En <sub>25.7-27.9</sub> Wo <sub>33.7-44.8</sub> Fs <sub>27.7-40.7</sub>	
Large Plagioclases (n=47)	47.4	0.02	32.3	<0.01	0.39	<0.01	0.10	16.9	1.65	0.16	n.d.	n.d.	n.d.	n.d.	99.00	An <sub>84.2</sub> Ab <sub>14.9</sub> Or <sub>0.9</sub>	An <sub>77.0-88.9</sub> Ab <sub>11.0-20.1</sub> Or <sub>0.1-2.9</sub>	
Plagioclases mesostasis (n=5)	51.0	0.03	30.1	0.02	0.65	<0.01	0.04	14.6	2.49	0.44	n.d.	n.d.	n.d.	n.d.	99.42	An <sub>74.4</sub> Ab <sub>23.0</sub> Or <sub>2.6</sub>	An <sub>77.7-76.8</sub> Ab <sub>20.4-24.9</sub> Or <sub>2.0-3.5</sub>	
Secondary Plagioclase (n=17)	43.0	n.d.	35.7	n.d.	1.38	n.d.	0.12	19.7	0.12	<0.01	n.d.	n.d.	n.d.	n.d.	100.00	An <sub>98.6</sub> Ab <sub>1.3</sub> Or <sub>0.1</sub>	An <sub>97.2-100</sub> Ab <sub>0-2.8</sub> Or <sub>0-0.3</sub>	
<b>Minor phases</b>																		
Chromite (n=5) <sup>§</sup>	<0.1	3.2	12.6	47.9	33.9	0.76	0.84	<0.1	n.d.	n.d.	n.d.	n.d.	n.d.	n.d.	99.78			
Ilmenite (n=13) <sup>§</sup>	<0.1	53.7	n.d.	<0.1	44.1	1.17	0.53	n.d.	n.d.	n.d.	n.d.	n.d.	n.d.	n.d.	99.81			
Apatite (n=19)	<0.01	n.d.	n.d.	n.d.	0.72	n.d.	<0.01	54.1	<0.01	n.d.	41.8	n.d.	n.d.	0.11	99.23			
Zircon (n=10)	32.4	n.d.	n.d.	n.d.	1.58	0.02	n.d.	0.06	n.d.	n.d.	0.14	1.31	66.2	0.16	101.83			
Tridymite (n=7)	98.9	0.07	0.23	0.03	0.36	<0.01	<0.01	0.13	<0.01	0.02	n.d.	n.d.	n.d.	n.d.	99.20			
Fe-rich olivine veins (n=16)	31.9	<0.01	0.06	0.19	53.1	1.46	14.4	0.05	<0.01	<0.01	n.d.	n.d.	n.d.	n.d.	101.13	Fo <sub>32.5</sub> Fa <sub>67.5</sub>	Fo <sub>29-35</sub> Fa <sub>65-71</sub>	
Metal cores (n=13)	<b>Fe</b> 99.08	<b>Ni</b> <0.01	<b>Co</b> 0.16	<b>Cu</b> <0.02	<b>Cr</b> <0.02	<b>Zn</b> <0.01	<b>Ca</b> 0.05	<b>Si</b> 0.03	<b>Mg</b> <0.01	<b>Mn</b> <0.01	<b>Na</b> <0.01	<b>K</b> <0.02	<b>S</b> <0.02		99.33			

Data were obtained by EPMA; n.d. = not detected; \*all Fe as FeO; zircon: Al was always below detection limit, high Fe content probably caused by contamination from surrounding phases such as ilmenite and Fe-metal; apatites: Cl and F average values are 0.3 and 4.0 wt.%, respectively; <sup>§</sup> Data obtained by SEM; chromite: V<sub>2</sub>O<sub>3</sub> = 0.61 wt.%, ilmenite: V<sub>2</sub>O<sub>3</sub> = 0.3 wt.%; for ilmenite and chromite: Ni was always below detection limit.

Table 3. Major and trace element composition of NWA 5073, compared to Stannern, Bouvante, and Nuevo Laredo. Oxides in wt.%, trace elements in  $\mu\text{g/g}$ .  $\text{Eu}/\text{Eu}^*$  and  $\text{La}_n/\text{Yb}_n^*$  are calculated relative to CI average given by Evensen et al. (1978).

	<b>NWA 5073</b>	<b>Stannern</b>	<b>Bouvante</b>	<b>Nuevo Laredo</b>
Mass (g)	0.098	1.0	1.47	1.0 g
TiO <sub>2</sub>	0.77	1.08	1.06	0.94
Al <sub>2</sub> O <sub>3</sub>	10.38	12.26	11.60	12.36
Cr <sub>2</sub> O <sub>3</sub>	0.587	0.33	0.33	0.30
FeO	20.13	18.58	20.07	20.91
MnO	0.58	0.55	0.50	0.63
MgO	8.70	6.98	6.26	5.70
CaO	9.46	10.99	10.40	10.90
Na <sub>2</sub> O	0.52	0.56	0.56	0.48
K <sub>2</sub> O	0.09	0.09	0.10	0.06
P <sub>2</sub> O <sub>5</sub>	0.097	0.10	0.14	0.09
Li	11.06	12.39	13.51	11.68
Be	0.32	0.44	0.42	0.37
Sc	25.8	30.2	30.8	35.8
V	78.51	56.90	55.20	60.10
Co	8.04	3.83	7.00	2.87
Ni	1.32	1.1	0.33	3.70
Cu	2.43	5.07	0.88	0.25
Zn	0.98	2.80	1.42	1.17
Ga	1.14	1.51	1.6	1.69
Rb	0.34	0.58	0.61	0.37
Sr	2131	92.7	93.7	84.4
Y	22.17	32.13	33.00	26.22
Zr	70.1	101	99.6	70.0
Nb	6.85	8.20	7.74	5.38
Cs	0.008	0.016	0.023	0.017
Ba	176	52.65	56.17	39.03
La	4.18	5.58	5.65	3.85
Ce	10.59	14.4	14.37	10.10
Pr	1.57	2.15	2.18	1.52
Nd	7.79	10.76	10.79	7.64
Sm	2.42	3.48	3.46	2.57
Eu	0.617	0.840	0.786	0.768
Gd	3.18	4.44	4.47	3.44
Tb	0.561	0.787	0.793	0.614
Dy	3.62	5.24	5.37	4.13
Ho	0.78	1.15	1.15	0.920
Er	2.22	3.26	3.26	2.67
Yb	2.04	3.06	2.87	2.56
Lu	0.291	0.434	0.421	0.366
Hf	1.77	2.51	2.52	1.83
Ta	0.365	0.441	0.413	0.292
W	0.193	0.174	0.165	0.105
Pb	0.24	(1.59)	0.32	0.26
Th	0.548	0.700	0.699	0.488
U	0.162	0.177	0.182	0.116
Eu/Eu*	0.68	0.65	0.61	0.79
La <sub>n</sub> /Yb <sub>n</sub> *	1.38	1.23	1.33	1.02

Table 4. LA-ICP-MS data of silicates in NWA 5073. Results in µg/g.

Pyroxene cores	1	2	3	4	5	6	7	8	single Px*	average (n=8)
La	0.010	0.025	0.005	0.005	0.013	0.007	0.021	0.008	0.366	0.012
Ce	0.032	0.058	0.027	0.016	0.047	0.024	0.050	0.028	1.302	0.035
Pr	0.009	0.013	0.004	0.004	0.010	0.004	0.010	0.008	0.276	0.008
Nd	0.066	0.081	0.027	0.029	0.068	0.032	0.063	0.064	1.726	0.054
Sm	0.068	0.054	0.020	0.037	0.059	0.020	0.048	0.050	0.883	0.044
Eu	0.011	0.008	0.004	0.007	0.008	0.005	0.009	0.008	0.054	0.007
Gd	0.127	0.143	0.038	0.062	0.098	0.055	0.095	0.117	1.486	0.092
Dy	0.244	0.240	0.067	0.131	0.169	0.096	0.171	0.228	2.297	0.168
Er	0.235	0.219	0.060	0.118	0.148	0.099	0.154	0.208	1.597	0.155
Yb	0.295	0.290	0.072	0.151	0.184	0.149	0.221	0.270	1.865	0.204
Lu	0.055	0.051	0.013	0.025	0.031	0.023	0.038	0.045	0.281	0.035
Plagioclase	1	2	3	4	5	6	7	average (n=7)		
La	0.243	0.350	0.522	0.308	0.328	0.286	0.194	0.319		
Ce	0.523	0.834	1.029	0.602	0.692	0.702	0.397	0.683		
Pr	0.064	0.101	0.124	0.076	0.087	0.088	0.053	0.085		
Nd	0.295	0.463	0.584	0.323	0.388	0.400	0.254	0.387		
Sm	0.099	0.133	0.164	0.095	0.089	0.126	0.081	0.112		
Eu	2.006	2.100	2.528	1.950	1.980	2.074	1.930	2.081		
Gd	0.067	0.124	0.154	0.082	0.083	0.101	0.064	0.096		
Dy	0.052	0.120	0.157	0.078	0.069	0.123	0.047	0.092		
Er	0.022	0.054	0.071	0.046	0.040	0.062	0.028	0.046		

\* single small, Fe-rich pyroxene, found in close association to a mesostasis area; not used for average pyroxene calculation.

Table 5. U and Th concentrations, calculated  $\alpha$ -decay dose, and frequencies and linewidths (FWHM) of the  $\nu_3(\text{SiO}_4)$ . Raman band of analyzed zircon grains from the NWA 5073 eucrite.

Zircon no.	U (ppm)	$\pm 2\sigma$	Th (ppm)	$\pm 2\sigma$	Dose ( $10^{16}$ $\alpha$ -events/mg)*	$\pm 2\sigma$ * <sup>1</sup>	Frequency ( $\text{cm}^{-1}$ )* <sup>2</sup>	FWHM ( $\text{cm}^{-1}$ )* <sup>2</sup>
Z1	<23	-	<20	-	<0.067		1000.5	9.9
Z3	<30	-	<20	-	<0.086		1001.2	8.5
Z4	<29	-	24	21	<0.093		1003.2	7.6
Z5	71	29	42	21	0.243	0.091	996.8	17.2
Z6	123	29	71	21	0.421	0.092	996.6	21.6
Z8	78	30	<21	-	0.255	0.096	999.3	12.1
Z9	105	29	86	21	0.372	0.092	998.2	18.8
Z10	75	30	<21	-	0.246	0.096	997.9	17.9
Z11	104	29	<21	-	0.334	0.092	997.2	25.8
Z13	160	29	120	21	0.559	0.092	991.7	25.3

\*The dose was calculated for an inferred age of 4555 Ma; \*<sup>1</sup>Errors do not include the error of the inferred age;

1018  
 1019  
 1020  
 1021  
 1022  
 1023  
 1024  
 1025  
 1026  
 1027  
 1028  
 1029  
 1030  
 1031  
 1032  
 1033

1034 **Figure Captions:**

1035

1036 **Fig. 1:** (a) Sawn surface of a section from the 185 g main mass of NWA 5073. (b) Thin section of  
1037 NWA 5073; transmitted light, crossed polarizers.

1038

1039 **Fig. 2:** Ternary phase diagram for pyroxenes (Px) analyzed in NWA 5073. Large pyroxenes preserved  
1040 their initial magmatic signature, as seen by Mg-enriched pigeonite cores. The chemical composition of  
1041 small pyroxenes is in the range of the rims of large pyroxene phenocrysts or even more Fe-enriched.  
1042 Pyroxenes found in the mesostasis are clearly distinct as they are significantly enriched in Ca. For  
1043 comparison, composition of pristine and metasomatized pyroxenes from NWA 2061 (dark gray, solid-  
1044 lined areas) and Y-75011 (light gray, dashed-lined areas) are shown, as these two eucrites also contain  
1045 secondary Ca-rich plagioclase. The latter data are taken from Barrat et al. (2011).

1046

1047 **Fig. 3:** BSE images of the bulk texture of NWA 5073 (a) and textural details of its Fe-rich olivine  
1048 veins (b-d). (a) Mosaic of BSE images from a NWA 5073. (b-d) Detailed images illustrating  
1049 prominent Fe-rich olivine veins that crosscut large pyroxene laths, while adjacent silicate grains are  
1050 devoid of them. (b) Typical zoned pyroxene lath with  $En_{57}Wo_5$  in the crystals core and  $En_{28}Wo_{17}$  at the  
1051 rim is crosscut by Fe-rich olivine veins that end abruptly towards adjacent plagioclases (Plg) and  
1052 smaller pyroxenes (Px). (c) Pyroxene-plagioclase border that shows a clear restriction of Fe-rich  
1053 olivine veins to large pyroxene crystals. (d) Enlarged Mg-rich core region of a large pyroxene lath that  
1054 is crosscut by Fe-rich olivine veins ( $Fe_{67}$ ) and Fe-diffusion pathways along cleavage planes. Olivine  
1055 veins are often occupied by small chromite, and troilite (FeS) grains, and Sr-sulfate inclusions, with  
1056 the latter being a weathering product. Fe-rich areas that are aligned parallel to the olivine veinlets are  
1057 probably formed by solid-state Fe-diffusion.

1058

1059 **Fig. 4:** BSE images of secondary phases in NWA 5073. (a) and (b): Fe-rich olivine veins (Ol) in large  
1060 pyroxene (Px) and Fe-diffusion paths into their pyroxene host along cleavage planes: Cc = calcite  
1061 (terrestrial weathering). (c) and (d): Secondary, Ca-rich plagioclase typically 5-20  $\mu$ m in diameter that  
1062 were usually found in close association with Fe-rich olivine veins (Ol), are highlighted in ellipses.  
1063 They are chemically distinct to adjacent large plagioclase (Plg).

1064

1065 **Fig. 5:** Ternary feldspar diagram illustrating three distinct plagioclase (Plg) types. Small plagioclase  
1066 grains, located in the mesostasis, are slightly more Ab-rich ( $An_{72-77}$ ) compared to larger plagioclase  
1067 laths, which scatter to slightly higher An values ( $An_{72-89}$ ). Secondary plagioclase is extremely enriched  
1068 in Ca with  $An_{97-100}$ .

1069

1070 **Fig. 6:** BSE images (a) and (c) of representative zircon grains (Zr), selected for  $\mu$ -Raman spectroscopy  
1071 and EPMA analyses. Zircon grains typically occur in association with ilmenite (Ilm), plagioclase  
1072 (Plg), Ca-pyroxene (Ca-Px), and silica ( $SiO_2$ ). Corresponding cathodoluminescence images are given  
1073 in (b) and (d). Zircon positions are highlighted as dashed areas.

1074

1075 **Fig. 7:** Diagram for bulk rock  $TiO_2$  vs.  $FeO_{total}/MgO$  of basaltic, including residual, eucrite samples.  
1076 The field of the basaltic eucrites has been drawn from a compilation of more than 170 analyses mainly  
1077 from Warren et al. (2009), references listed in Barrat et al. (2007), and the residual eucrites from  
1078 Yamaguchi et al. (2009). Residual eucrites cannot be distinguished from the basaltic eucrites in this  
1079 diagram.

1080

1081 **Fig. 8:** Rare Earth Element (REE) abundances relative to CI chondritic abundance (Evensen et al.,  
1082 1978), given for NWA 5073 bulk rock in comparison to Stannern, NWA4523, Juvinas, and Nuevo  
1083 Laredo.

1084

1085 **Fig. 9:** Trace element pattern for NWA 5073 bulk rock compared to the Stannern-trend eucrites,  
1086 including Stannern and NWA 4523, and Nuevo Laredo and Juvinas eucrites. All data are given  
1087 relative to the Juvinas eucrite. Sr and Ba values of NWA 5073 whole rock are high (2131 and 176  
1088 ppm, respectively), probably due to terrestrial weathering (Stelzner et al., 1999) and thus are excluded  
1089 from this diagram.

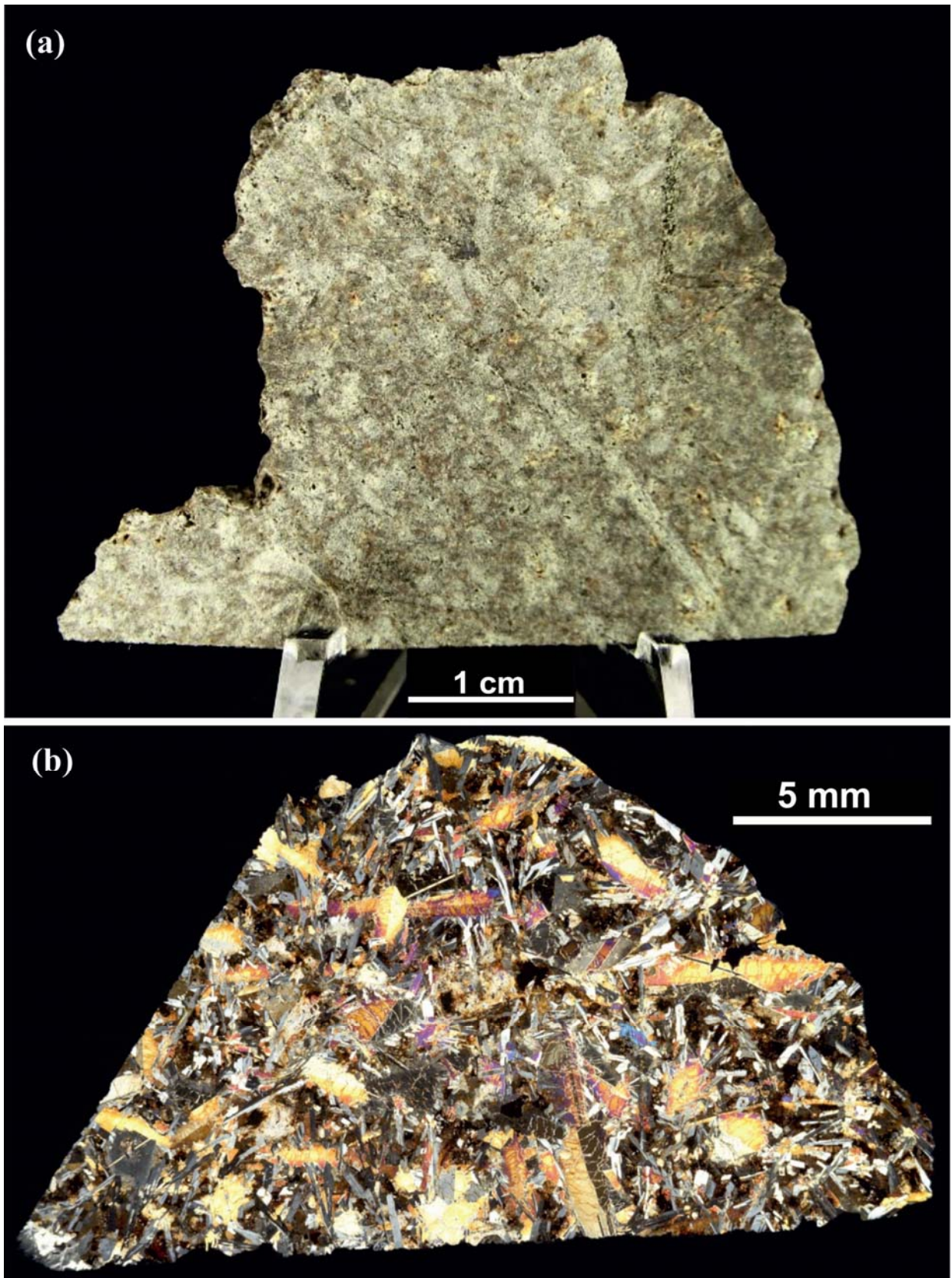
1090  
1091  
1092  
1093  
1094  
1095  
1096  
1097  
1098  
1099  
1100  
1101  
1102  
1103  
1104  
1105  
1106  
1107  
1108  
1109  
1110  
1111  
1112  
1113  
1114  
1115  
1116  
1117  
1118  
1119  
1120  
1121  
1122  
1123  
1124  
1125  
1126  
1127  
1128  
1129  
1130  
1131  
1132  
1133  
1134  
1135  
1136  
1137  
1138  
1139

**Fig. 10:** REE pattern for plagioclase and pyroxene grains analyzed in NWA 5073. Average plagioclase (n=7) is shown by black squares, minimum and maximum values of all analyzed plagioclase grains are reported within the data range highlighted in light gray. The average of pigeonite cores (n=8) is given by white triangles. Data range for all analyzed pigeonite cores is highlighted in dark gray. One single small, Fe-rich pyroxene (light gray circles), closely associated with a mesostasis area, is extremely enriched in REE (Lu 10×CI). This analysis has not been used for average pyroxene core calculation.

**Fig. 11:** Oxygen isotope data for NWA 5073 compared to other eucrites (monomict, polymict, and cumulate eucrites), howardites, diogenites, and angrites.  $\Delta^{17}\text{O}$  values are linearized (Miller, 2002). In this  $\Delta^{17}\text{O}$  versus  $\delta^{18}\text{O}$  diagram, samples formed from a homogeneous reservoir that subsequently fractionated by mass-dependent processes, plot along horizontal lines. Silicate minerals on Earth have isotopic compositions consistent with mass-dependent fractionation from a single reservoir, and define the terrestrial fractionation line (TFL). Angrites define a second horizontal line, the angrite fractionation line (AFL), with a mean  $\Delta^{17}\text{O}$  value of  $-0.072 \pm 0.007$  ( $1\sigma$ ). If polymict breccias are excluded, remaining HED samples also show limited  $\Delta^{17}\text{O}$  variation and define a single eucrite fractionation line (EFL) with a mean  $\Delta^{17}\text{O}$  value of  $-0.239 \pm 0.007$  ( $1\sigma$ ). Diagram modified after Greenwood et al. (2005).

**Fig. 12:** Representative Raman spectra of five single zircon grains in sample NWA 5073 reveal a decreased frequency and an increased broadening of the  $\nu_3(\text{SiO}_4)$  stretching band near  $\sim 1008 \text{ cm}^{-1}$  (dashed line) with increasing radiation dose ( $D$ ). The calculated  $\alpha$ -dose, given within  $2\sigma$  uncertainties, and expressed per  $10^{16} \times \alpha$ -decay events/mg sample, is shown close to the spectra for each zircon crystal. Single zircon analyses are presented relative to a pure, synthetic, crystalline zircon (gray), taken from the RRUFF Raman data base.

**Fig. 13:** (a) Diagram of the frequency of the  $\nu_3(\text{SiO}_4)$  band analyzed in ten zircon crystals in NWA 5073 plotted against the measured linewidth of this band (given as full width at half maximum, FWHM). The radiation damage trend (RDT, gray field) is defined by variably, self-irradiation-damaged, terrestrial zircons (Saxonian rhyolites and Sri Lanka zircons data from Nasdala et al., 1998; 2004; Zhang et al., 2001a, b; own unpubl. data). A synthetic, non-metamict zircon is also plotted. Recent episodic annealing of heavily metamict zircon would shift the data points to the upper right in this diagram (highlighted by arrows), as indicated by dry heating experiments (Geisler et al., 2001; Geisler, 2002). (b) Plot of the linewidth (FWHM) of the  $\nu_3(\text{SiO}_4)$  band vs. the  $\alpha$ -decay dose (calculated accumulated radiation dose) for all analyzed zircon grains in NWA 5073. Uncertainties are in the range of  $2\sigma$ . All data points plot below the radiation damage accumulation curve defined by Palenik et al. (2003), unambiguously indicating post-crystallization thermal annealing. Note that annealing of the NWA 5073 zircons is also obvious when compared with the Saxonian rhyolite zircons, which have neither episodically nor continuously been annealed (Nasdala et al., 1998) and were used to determine the damage accumulation curve. For more details of how the damage accumulation curve was defined see Palenik et al. (2003).

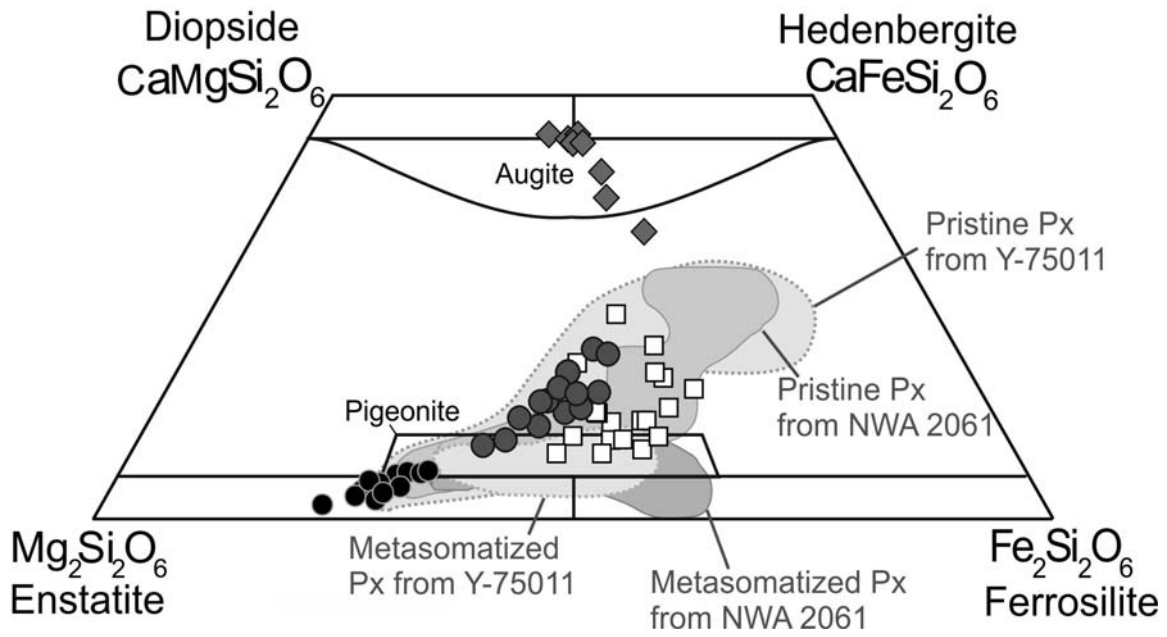


1140  
1141  
1142  
1143  
1144

Fig.1

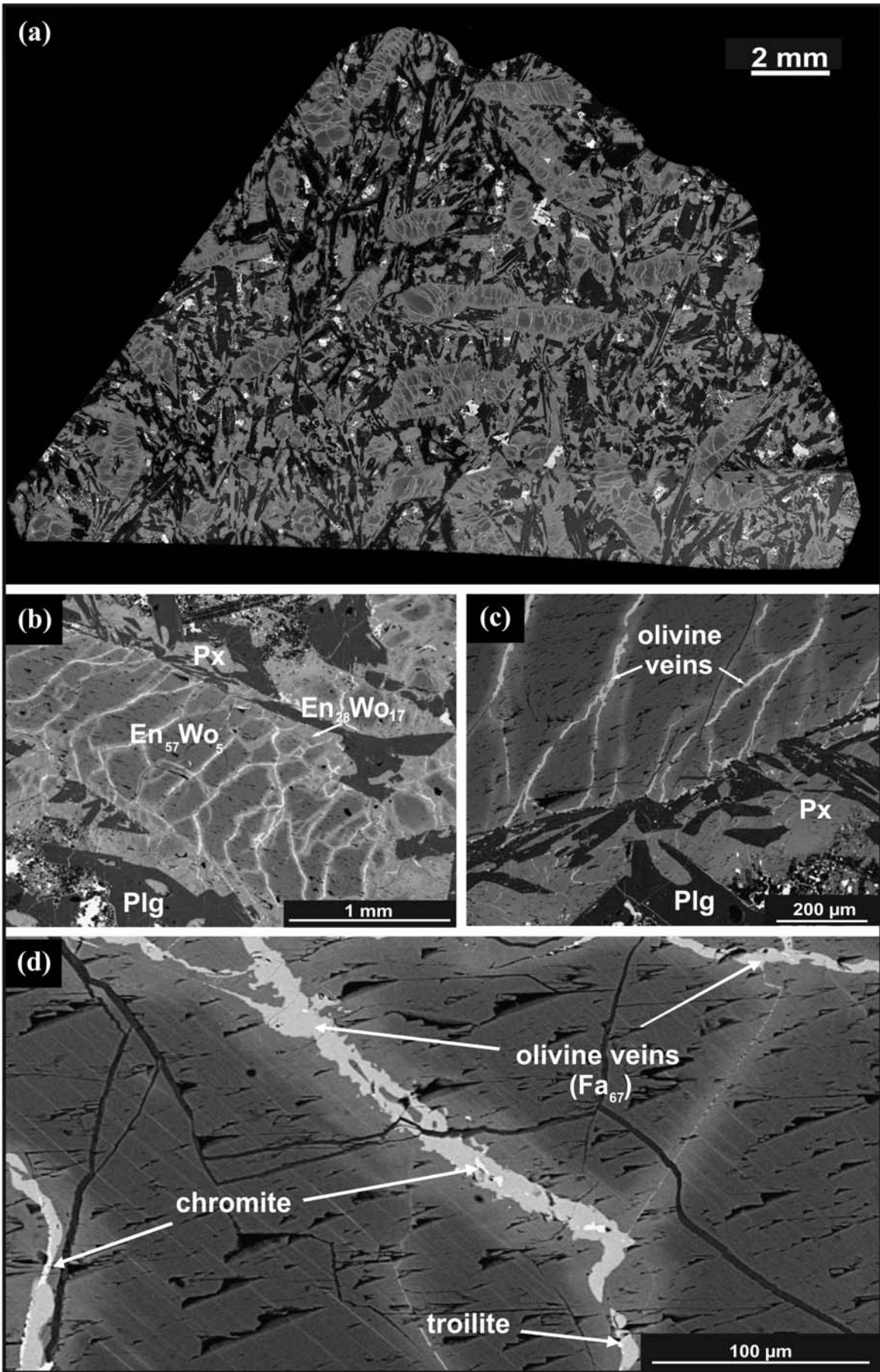


- Large Px (cores)     ◆ Ca-Px (mesostasis)
- Large Px (rims)     □ Small Px



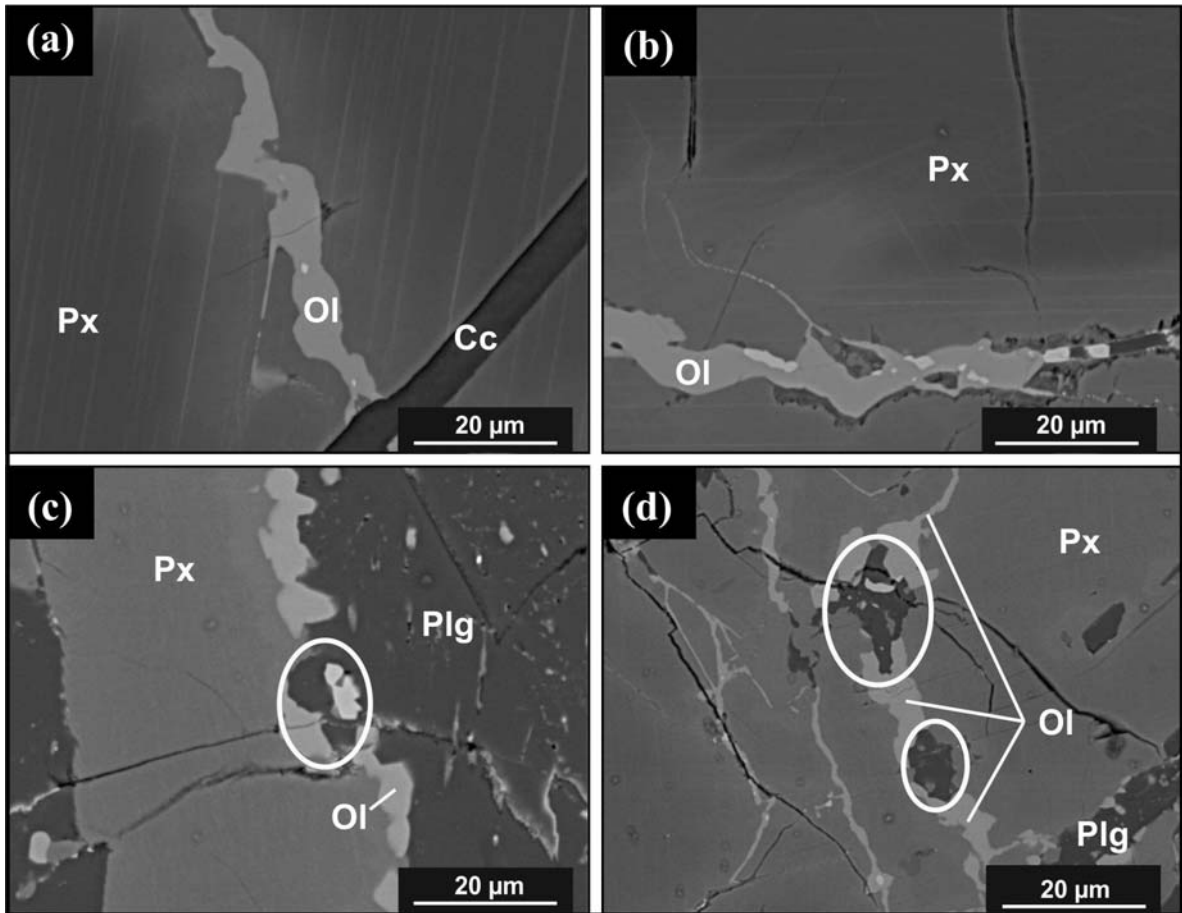
1145  
1146  
1147  
1148  
1149

Fig.2



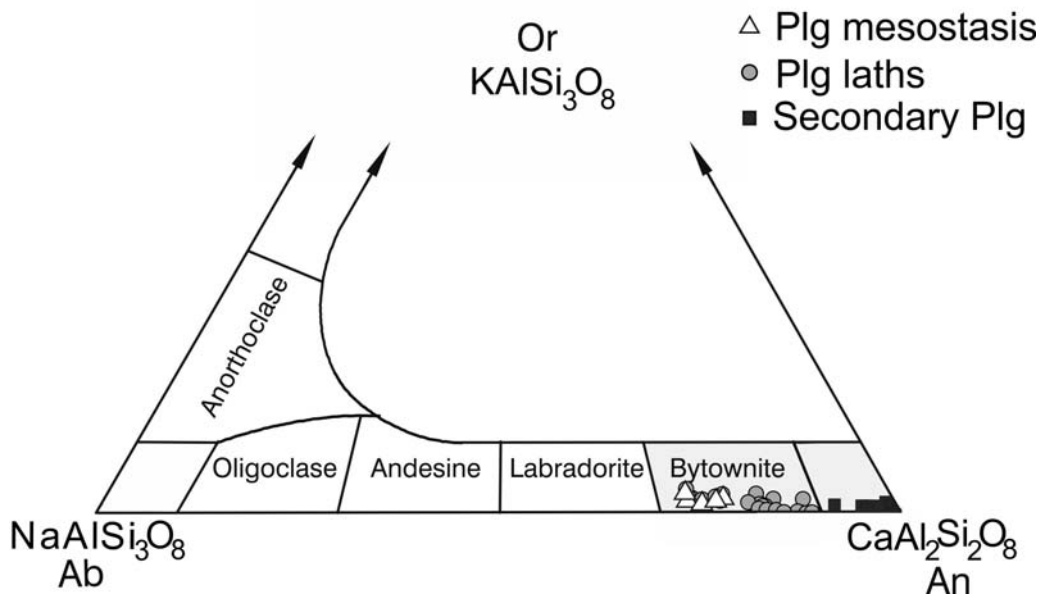
1150  
1151  
1152

Fig.3



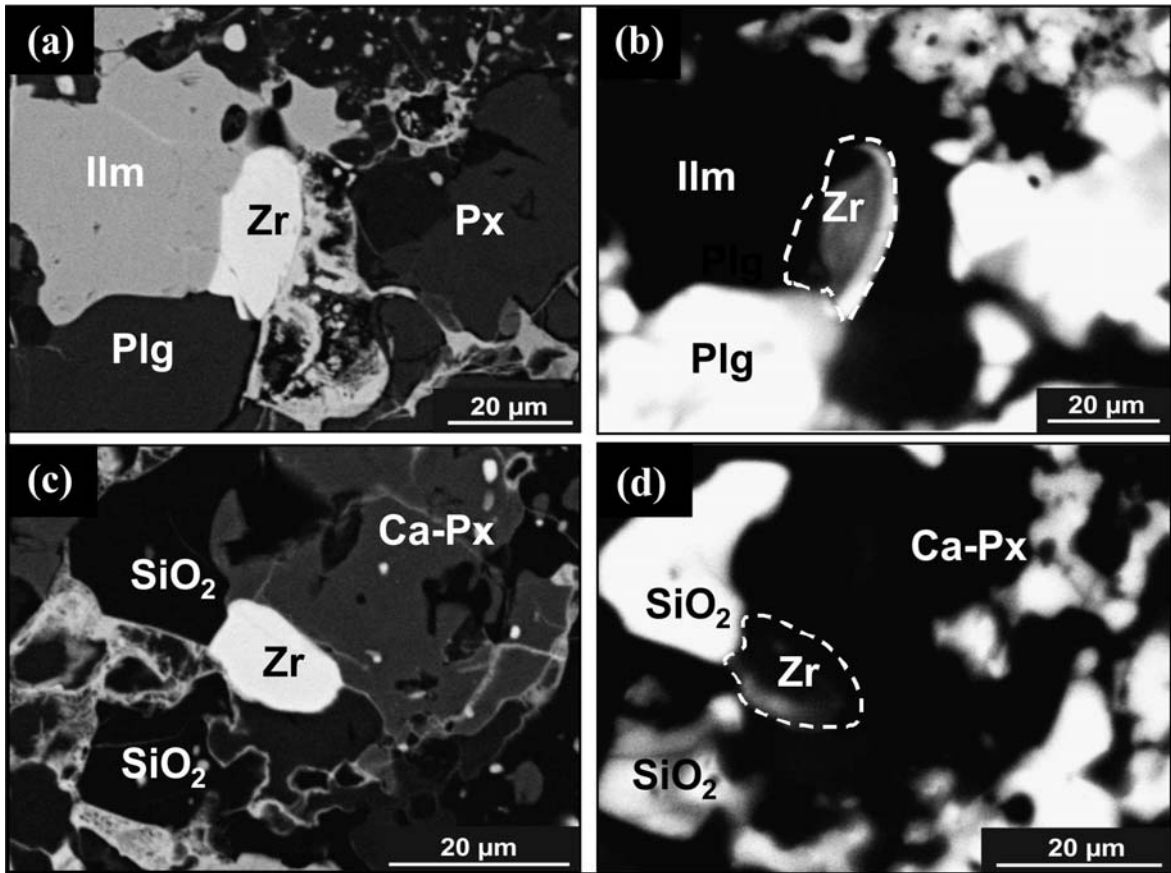
1153  
1154  
1155  
1156

Fig.4



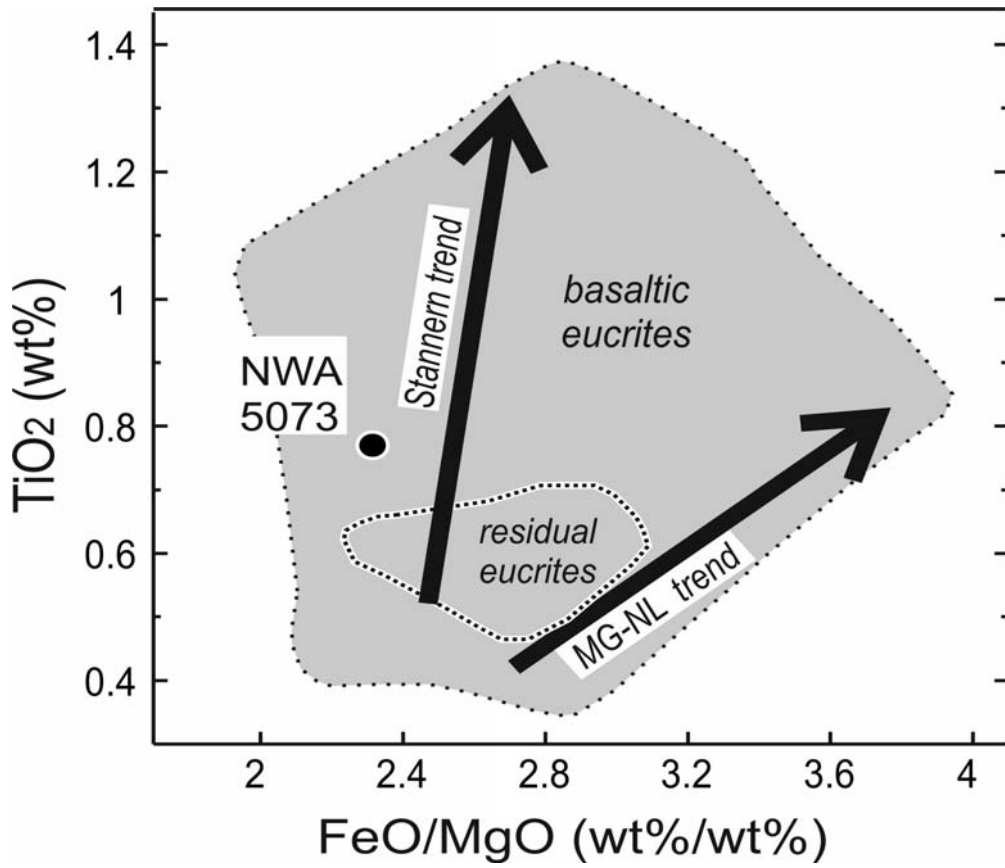
1157  
1158  
1159

Fig.5



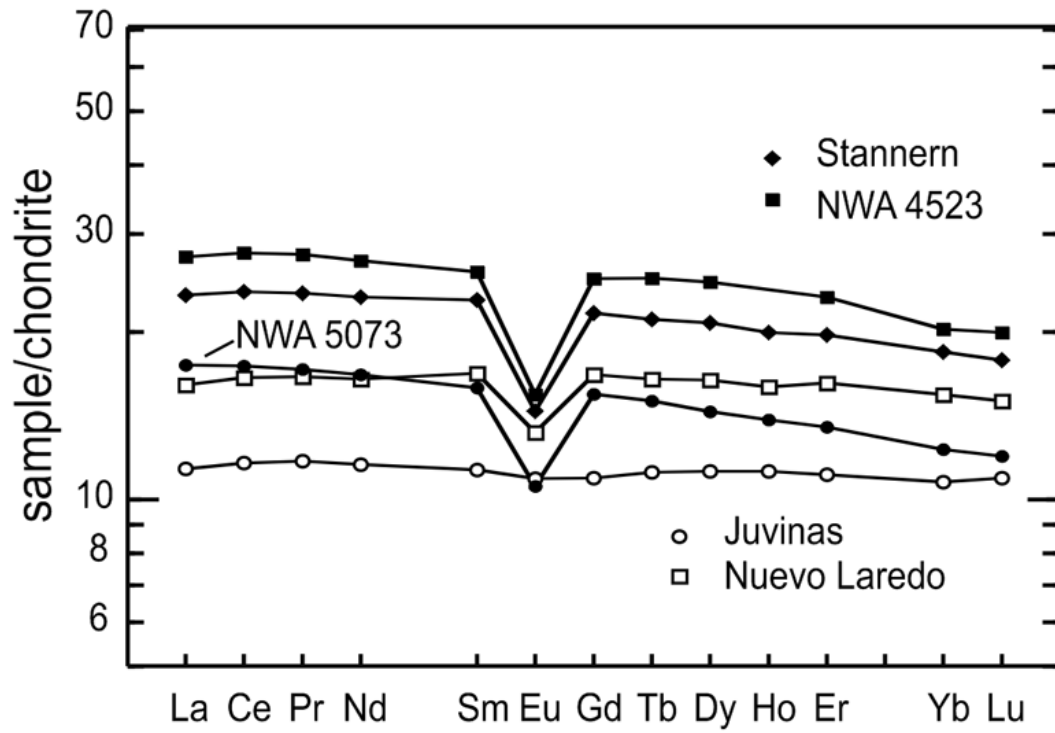
1160  
1161  
1162  
1163

Fig.6

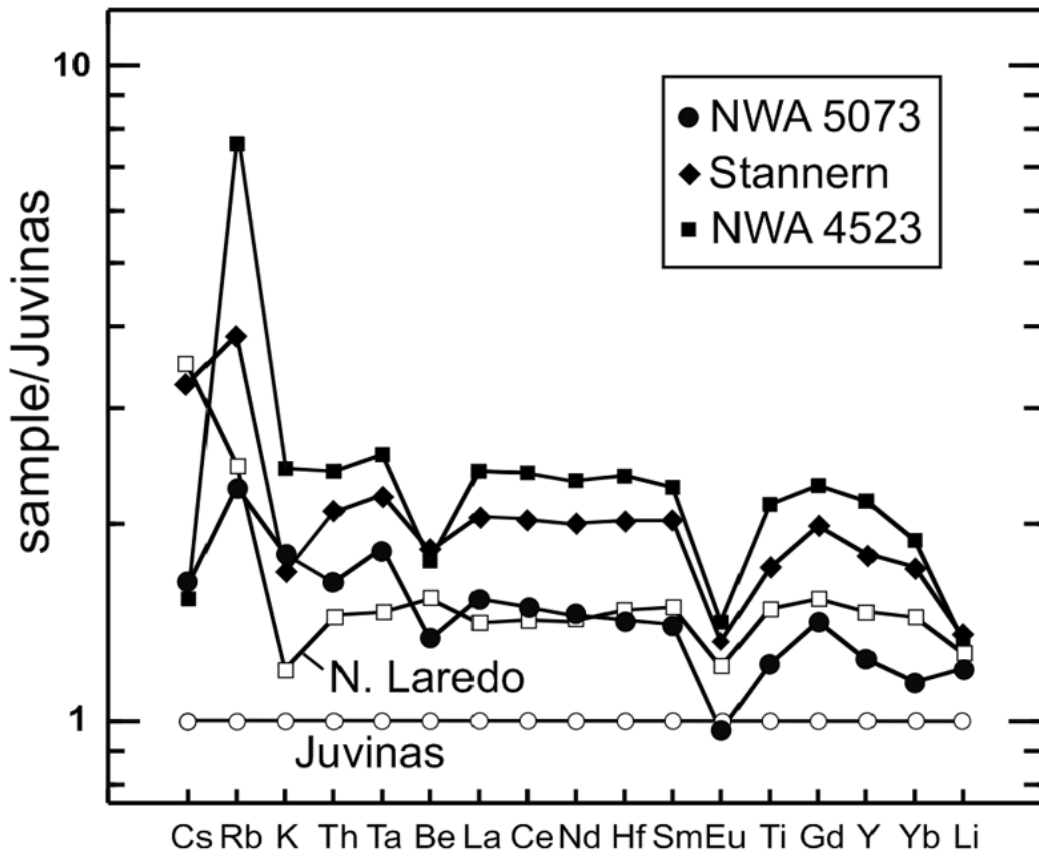


1164  
1165  
1166

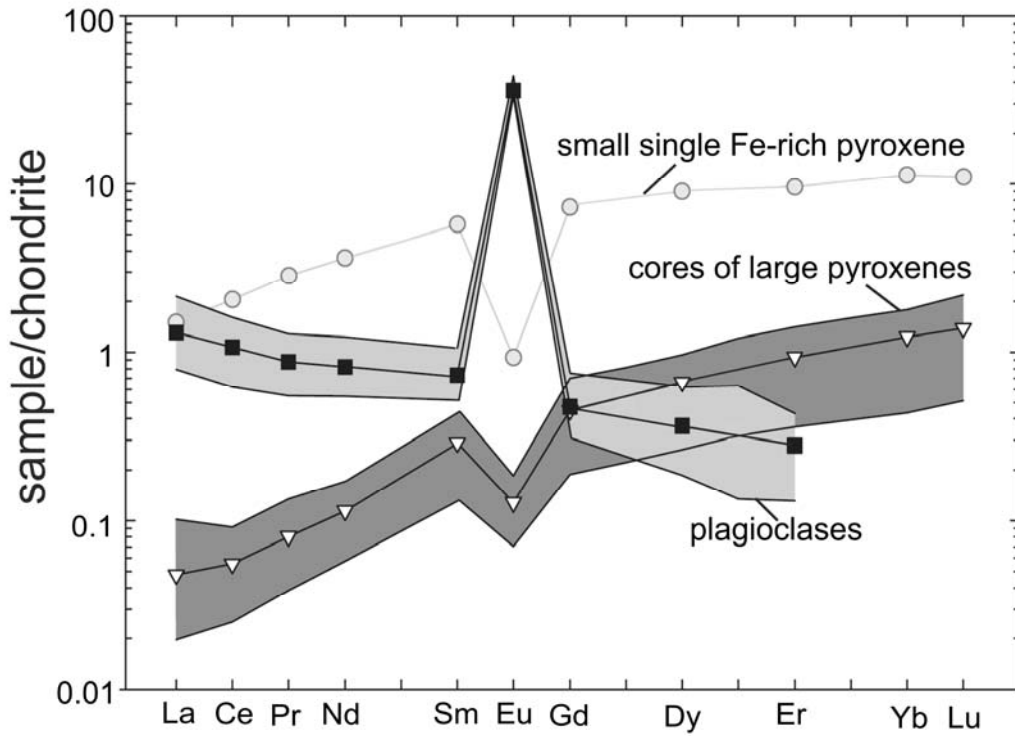
Fig.7



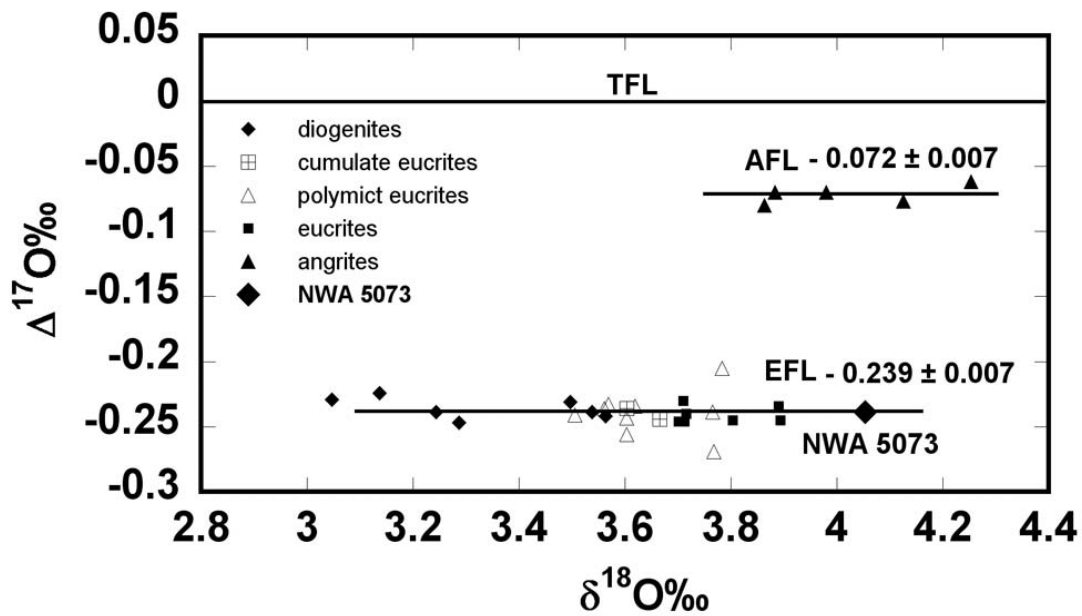
1167  
1168 Fig.8  
1169  
1170



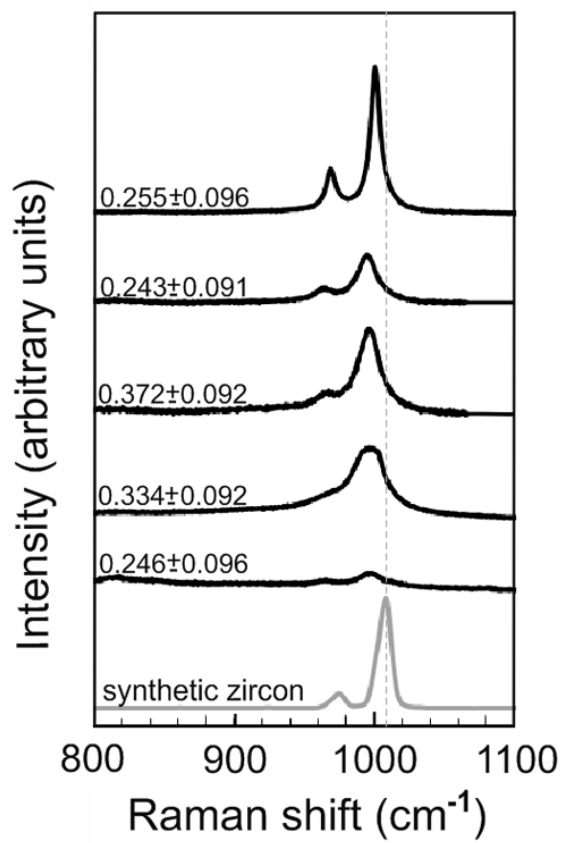
1171  
1172 Fig.9  
1173  
1174



1175  
1176 Fig.10  
1177



1178  
1179 Fi.11  
1180  
1181  
1182  
1183  
1184



1185  
1186  
1187  
1188  
1189  
1190

Fig.12

